

Hawking time crystals

Juan Ramón Muñoz de Nova and Fernando Sols

Departamento de Física de Materiales, Universidad Complutense de Madrid, E-28040 Madrid, Spain

(Dated: October 20, 2025)

We propose a time crystal based on a quantum black-hole laser, where the genuinely spontaneous character of the symmetry breaking stems from the self-amplification of spontaneous Hawking radiation. The resulting Hawking time crystal (HTC) is characterized by the periodic dependence of the out-of-time density-density correlation function, while equal-time observables are time-independent because they embody averages over different realizations with a random oscillation phase. The HTC can be regarded as a nonlinear periodic analogue of the Andreev-Hawking effect, exhibiting anticorrelation bands resulting from the spontaneous, quantum emission of pairs of dispersive waves and solitons into the upstream and downstream regions. Remarkably, the time-crystal formation is understood in terms of two time operators: one associated to the initial black-hole laser and another associated to the final spontaneous Floquet state.

Introduction.— The field of analogue gravity [1] investigates the simulation of otherwise inaccessible gravitational phenomena by using a variety of tabletop experiments, including atomic condensates [2, 3], nonlinear optical fibers [4, 5], ion rings [6, 7], water waves [8, 9], quantum fluids of light [10, 11], superconducting qubits [12], or superfluid helium [13]. This has resulted in observations of the dynamical Casimir effect [14], Sakharov oscillations [15], superradiance [16], inflation [17], Unruh effect [18], quasinormal ringdown [19], backreaction [20], or cosmological particle creation [21, 22]. A central topic is the observation of spontaneous Hawking radiation [23–38], finally achieved in atomic condensates [39–41], manifested as the correlated quantum emission of Bogoliubov quasiparticles from a subsonic/supersonic interface playing the role of the event horizon. Since scattering within the supersonic region also provides a bosonic analogue of the Andreev effect [42], by borrowing concepts from quantum optics [43, 44] the whole process can be understood as a joint Andreev-Hawking effect [45].

A major remaining challenge is the observation of a black-hole laser (BHL) [46–63], where Hawking radiation is self-amplified by successive reflections between a pair of horizons. Of particular interest is the late-time behavior of a BHL, after the initial instability has saturated, where it may exhibit a periodic regime of continuous emission of solitons (CES) [55, 59], representing the *bona-fide* BHL [55]. Indeed, the CES state is a universal feature of flowing condensates, providing one of the simplest realizations of the more general concept of spontaneous Floquet state: a state of a time-independent Hamiltonian which oscillates like a Floquet state due to interactions [64]. Among other intriguing features, spontaneous Floquet states display a temporal Floquet-Nambu-Goldstone (FNG) mode with zero quasifrequency, whose quantum amplitude represents a rare tangible realization of time operator in Quantum Mechanics [65]. This connects with the field of time crystals [66–68], where both discrete [69–73] and continuous [74–78] time crystals have been achieved in a variety of systems [79–93].

So far, spontaneous Floquet states have emerged only within mean-field descriptions, imposing a global time origin. Hence, even though there is a temporal FNG mode, technically speaking the symmetry breaking of time-translation invariance is not truly spontaneous. Here we show that a *bona-fide* continuous time crystal can be achieved in a spontaneous Floquet state by leveraging the quantum nature of the spontaneous Hawking radiation self-amplified in a BHL, thus denoted as a Hawking time crystal (HTC). We prove that the initial BHL also has an associated time operator by exploiting its description as a degenerate parametric amplifier (DPA) [36, 45, 51], whose behavior determines the asymptotic time-crystallization. Furthermore, we argue that an HTC provides a nonlinear periodic counterpart of the Andreev-Hawking effect.

BHL model.— We take the flat-profile BHL (FPBHL) model as test ground since, due to its simplicity, it neatly captures the physics at play in more realistic scenarios [25, 27, 53, 55, 63]. For $t < 0$, a 1D homogeneous atomic quasicondensate [94] flows from left to right, described by a stationary Gross-Pitaevskii (GP) wavefunction $\Psi_0(x) = \sqrt{n_0}e^{iqx}$, whose flow and sound speeds are $v = \hbar q/m < c_0 = \sqrt{gn_0/m}$, where g is the coupling constant describing the short-ranged interactions between atoms and m is their mass. Hereafter, $\hbar = m = c_0 = 1$, and the GP wavefunction is rescaled as $\Psi(x, t) \rightarrow \sqrt{n_0}\Psi(x, t)$. For $t \geq 0$, the external potential and the coupling constant are inhomogeneously quenched so that the condensate becomes supersonic for $|x| < L/2$, with sound speed $c_2 < v$, while $\Psi_0(x)$ remains stationary. Hence, a BHL configuration is reached, presenting two sonic horizons at $x = \pm L/2$, Fig. 1a.

A BHL is characterized by a finite Bogoliubov spectrum of complex frequencies. We focus on short cavities containing only one degenerate unstable mode with purely imaginary frequency $i\Gamma$, whose quantum amplitude \hat{X} behaves as the position operator in a DPA (see Appendix). This optimal cavity choice both maximizes Γ and minimizes the transient towards the final state

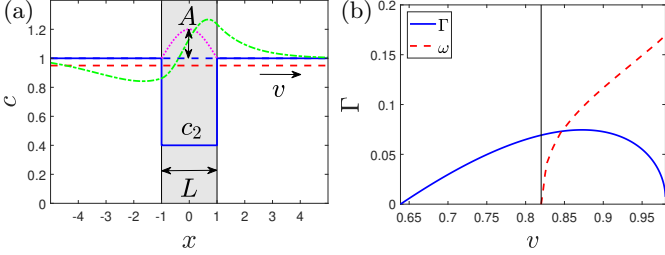


FIG. 1. (a) Sound (solid blue) and flow (dashed red) velocity profile of the FPBHL at $t = 0$. Horizontal dashed blue line represents the initial homogeneous condensate $\Psi_0(x) = e^{ivx}$. The shaded area indicates the supersonic lasing cavity where the coupling constant is quenched for $t \geq 0$ so that $c(x) = c_2$. A perturbation of amplitude A (dotted magenta) is added to the initial GP condition as classical seed for the unstable mode (dashed-dotted green). (b) Velocity dependence of Γ (solid blue) and ω (dashed red) for $c_2 = 0.4$, $L = 2$. Vertical line indicates $v = v_c$.

[53, 55, 63]. In a BHL, quantization spontaneously breaks time-translation symmetry due to the absence of a well-defined instantaneous vacuum [36]. Based on this observation, we prove that any DPA has associated a time operator [95].

Once excited, the lasing mode is exponentially amplified up to the saturation regime, where interactions become critical. In general, a condensate flowing over some obstacle with velocity v exhibits a dynamical phase diagram [96–98] where, above certain critical velocity v_c , it asymptotically approaches the CES state [64],

$$\Psi(x, t) \xrightarrow[t \rightarrow \infty]{} e^{-i\mu t} \Psi_0(x, t), \quad (1)$$

μ being the quasichemical potential and $\Psi_0(x, t)$ a periodic wavefunction, $\Psi_0(x, t) = \Psi_0(x, \phi_0 + \omega t)$, with $\Psi_0(x, \phi + 2\pi) = \Psi_0(x, \phi)$ and $\omega = 2\pi/T$. The velocity dependence of Γ, ω for a FPBHL is shown in Fig. 1b. Due to the time-independence of the underlying Hamiltonian, the CES state is a spontaneous Floquet state, where the oscillation phase-shift ϕ_0 is not *a priori* fixed, in contrast to conventional Floquet systems. This leads to the emergence of a temporal FNG mode in the Bogoliubov spectrum, whose quantum amplitude \hat{t}_0 is the time operator describing the quantum fluctuations of the global time-shift $t_0 = -\phi_0/\omega$ [65]. However, at the mean-field level, ϕ_0 is still fixed by the deterministic GP equation once an initial condition is set.

Hawking time crystal.— In order to achieve a genuine spontaneous temporal symmetry breaking, we go beyond mean-field by exploring the classical-quantum crossover of a BHL [63]. Specifically, we add a small perturbation within the lasing cavity (dotted magenta in Fig. 1a), so the initial GP wavefunction at $t = 0$ now reads $\Psi(x, 0) = [1 + A\delta\Psi_C(x)] e^{ivx}$, with $\delta\Psi_C(x) = \cos(\pi x/L)\theta(x + L/2)\theta(L/2 - x)$ and θ the Heaviside function. This classical seed provides a coherent ampli-

tude to the lasing mode (dashed-dotted green), mimicking the effect of Bogoliubov-Cherenkov-Landau radiation [99] in real experiments [41, 62, 100, 101]. As quantum state, we take the initial quasiparticle vacuum. For large A , the dynamics is described by a Bogoliubov approximation of small quantum fluctuations around the mean-field GP trajectory generated by the amplification of the initial classical seed. For small A , the dynamics is governed by the squeezing of the initial quantum vacuum, representing the self-amplification of spontaneous Hawking radiation. Hence, A is a control parameter of the classical-quantum crossover.

The time evolution of both the condensate and its quantum fluctuations is computed via the Truncated Wigner (TW) method [102], a quantum Monte Carlo technique used in both analogue gravity [25, 40, 63, 103, 104] and time crystals [88, 105]; here we consider ensembles of $N_{\text{stat}} = 1000$ simulations [95]. We evaluate the ensemble-averaged density

$$n(x, t) \equiv \langle \hat{n}(x, t) \rangle = \langle \hat{\Psi}^\dagger(x, t) \hat{\Psi}(x, t) \rangle, \quad (2)$$

and the second-order correlation function

$$g^{(2)}(x, x', t, t') \equiv \langle \hat{\Psi}^\dagger(x, t) \hat{\Psi}^\dagger(x', t') \hat{\Psi}(x', t') \hat{\Psi}(x, t) \rangle - n(x, t) n(x', t'). \quad (3)$$

We distinguish between the *equal-time* correlation function (ETCF) $g^{(2)}(x, x', t) \equiv g^{(2)}(x, x', t, t)$ and the *out-of-time* correlation function (OTCF) $g^{(2)}(x, x', \tau; t) \equiv g^{(2)}(x, x', t, t + \tau)$.

Figs. 2a-c, e-g show $n(x, t)$ and $g^{(2)}(x, x', t)$ for decreasing $A = 0.05, 0.005, 0$, respectively. For large A , Figs. 2a,e, a good agreement is found with the Bogoliubov prediction [65]

$$\begin{aligned} n(x, t) &\simeq n_0(x, t) \equiv |\Psi_0(x, t)|^2, \\ g^{(2)}(x, x', t) &\simeq \partial_t n_0(x, t) \partial_t n_0(x', t) C(t). \end{aligned} \quad (4)$$

The quadratic function $C(t) = \langle \hat{t}_0^2(t) \rangle$ is the CES time-operator variance, increasing in time due to frequency fluctuations (these are found negligible in our simulations). Using the phase-shift operator $\hat{\phi}_0 = -\omega \hat{t}_0$, spontaneous symmetry breaking requires $\Delta\phi_0 = \sqrt{\langle \hat{\phi}_0^2 \rangle - \langle \hat{\phi}_0 \rangle^2} \gtrsim 1$. This is achieved for a purely quantum BHL (i.e., $A = 0$), Figs. 2c,g, where there is no mean-field evolution and all the dynamics is due to quantum fluctuations, with ϕ_0 randomly chosen in each TW realization. If we assume a uniform distribution, ensemble averages then represent averages over $t_0 \in [0, T]$, resulting in time-independent values $n(x, t) = n_{\text{HTC}}(x)$ and $g^{(2)}(x, x', t) = g_{\text{HTC}}^{(2)}(x, x', \tau = 0)$, with

$$n_{\text{HTC}}(x) = \frac{1}{T} \int_0^T dt_0 n_0(x, t_0), \quad (5)$$

$$\begin{aligned} g_{\text{HTC}}^{(2)}(x, x', \tau) &= \frac{1}{T} \int_0^T dt_0 n_0(x, t_0 + \tau) n_0(x', t_0) \\ &\quad - n_{\text{HTC}}(x) n_{\text{HTC}}(x'). \end{aligned}$$

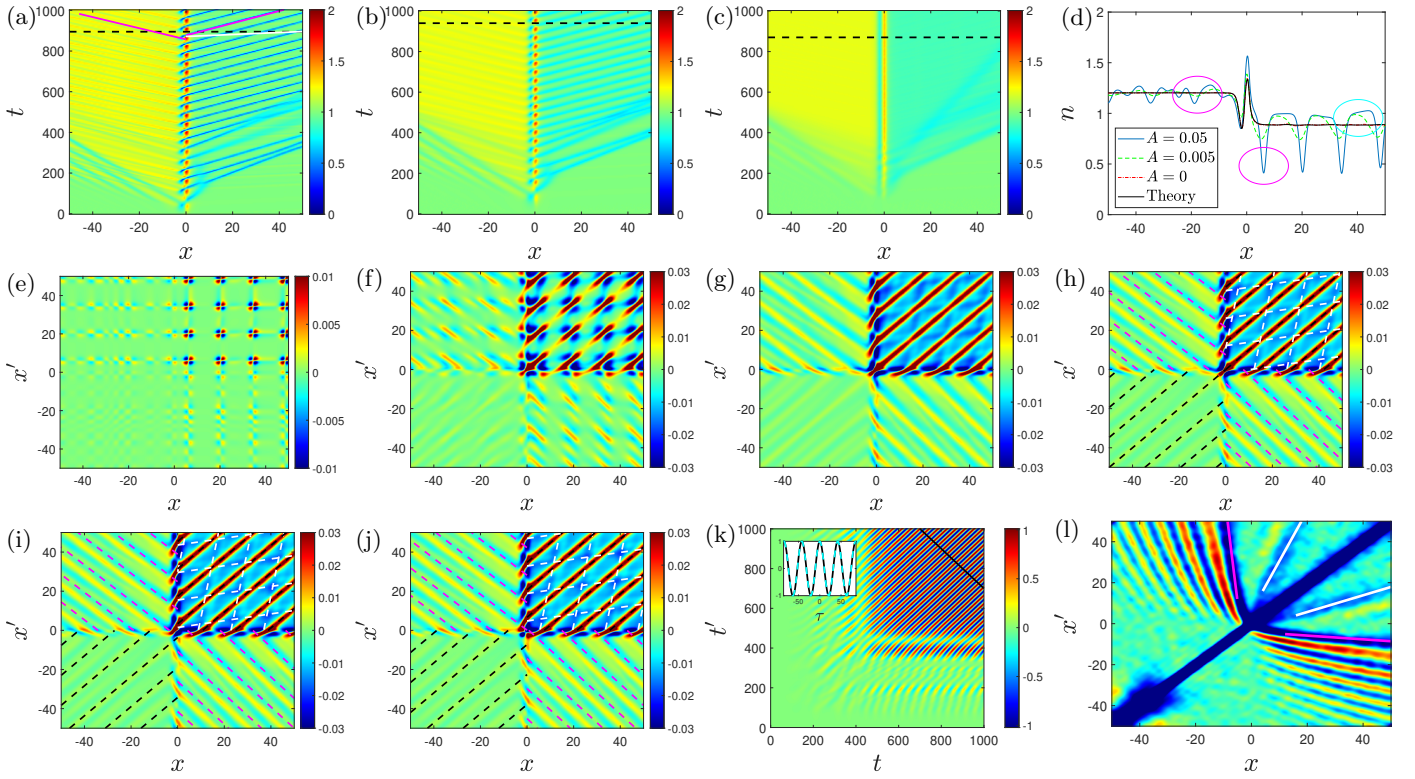


FIG. 2. Expectation values for a FPBHL with $v = 0.95, c_2 = 0.4, L = 2$, computed via TW method. (a)-(c) Ensemble-averaged density $n(x, t)$ for initial classical amplitudes $A = 0.05, 0.005, 0$, respectively. (d) Snapshots of $n(x, t)$ at the times indicated by horizontal dashed line in (a)-(c). Black line is the theoretical prediction $n_{\text{HTC}}(x)$, Eq. (5). (e)-(g) ETCF $g^{(2)}(x, x', t)$ for (a)-(c), evaluated at the times shown in (d). (h) Theoretical ETCF $g^{(2)}_{\text{HTC}}(x, x', \tau = 0)$, Eq. (5). Dashed lines indicate the expected correlation bands, Eqs. (6), (7). (i)-(j) OTCF $g^{(2)}(x, x', \tau; t)$ for $A = 0$, evaluated at $\tau = 10, 20$ and fixed $t = 870$. (k) $\text{Re } \mathcal{G}(t, t')$. Inset: 1D profile along the black line in the main plot. Dashed cyan is the theoretical prediction $\text{Re } \mathcal{G}_{\text{HTC}}(\tau) = \cos \omega \tau$. 1) Spatial structure of the ETCF for a flat-profile black hole with $v = 0.95, c_2 = 0.4$. Magenta (white) solid lines indicate the Hawking (Andreev) correlation bands.

An excellent agreement with this theoretical prediction is found at late times for both density (Figs. 2c,d) and ETCF (Figs. 2g,h).

The system periodicity is manifested through the OTCF, $g^{(2)}(x, x', \tau; t) = g^{(2)}_{\text{HTC}}(x, x', \tau) = g^{(2)}_{\text{HTC}}(x, x', \tau + T)$, displayed in Figs. 2i,j for $\tau = 10, 20$ and fixed $t = 870$. As figure of merit for the OTCF periodicity, we choose the peak of its spatial Fourier spectrum within the downstream-upstream quadrant, $\mathcal{G}(t, t')$ (see Appendix). The real part of $\mathcal{G}(t, t')$ is shown in Fig. 2k; the imaginary part displays a similar behavior [95]. At late times, $\mathcal{G}(t, t')$ becomes function solely of $\tau = t' - t$ (diagonal fringes). The inset shows the 1D profile along the perpendicular cut in the main plot, in great agreement with the HTC prediction $\mathcal{G}_{\text{HTC}}(\tau) = e^{i\omega\tau}$ [95] (dashed cyan).

The suppression of the time dependence of the density and the ETCF, as well as the periodic nature of the OTCF, are the characteristic hallmarks of a *bona-fide* time crystal [68], here revealing the formation of an HTC, i.e., a continuous time crystal whose spontaneous symmetry breaking results from the self-amplification of

spontaneous Hawking radiation.

Nonlinear Andreev-Hawking effect.— The spatial structure of the correlations in Fig. 2 reflects the underlying CES state, characterized by the periodic emission of dispersive waves/solitons into the upstream/downstream regions, well fitted by a ballistic trajectory $x_{u,d}(t) = x_{u,d}^{(0)} + v_{u,d}t$ (magenta lines, circles in Fig. 2a,d, respectively). Simultaneously, another traveling wave is emitted into the downstream region along $x_w(t) = x_w^{(0)} + v_w t$ (white line, cyan circle in Fig. 2a,d).

From Eq. (5), strong self-correlations between the upstream waves/downstream solitons and their past and future counterparts are predicted for the OTCF along the diagonals [95]

$$\frac{x' - x}{v_{u,d}} = \tau + nT, \quad n \in \mathbb{Z}, \quad (6)$$

dashed black lines in Figs. 2h-j. In turn, the density defect carried by a soliton is correlated with the positive amplitude of the upstream and downstream waves,

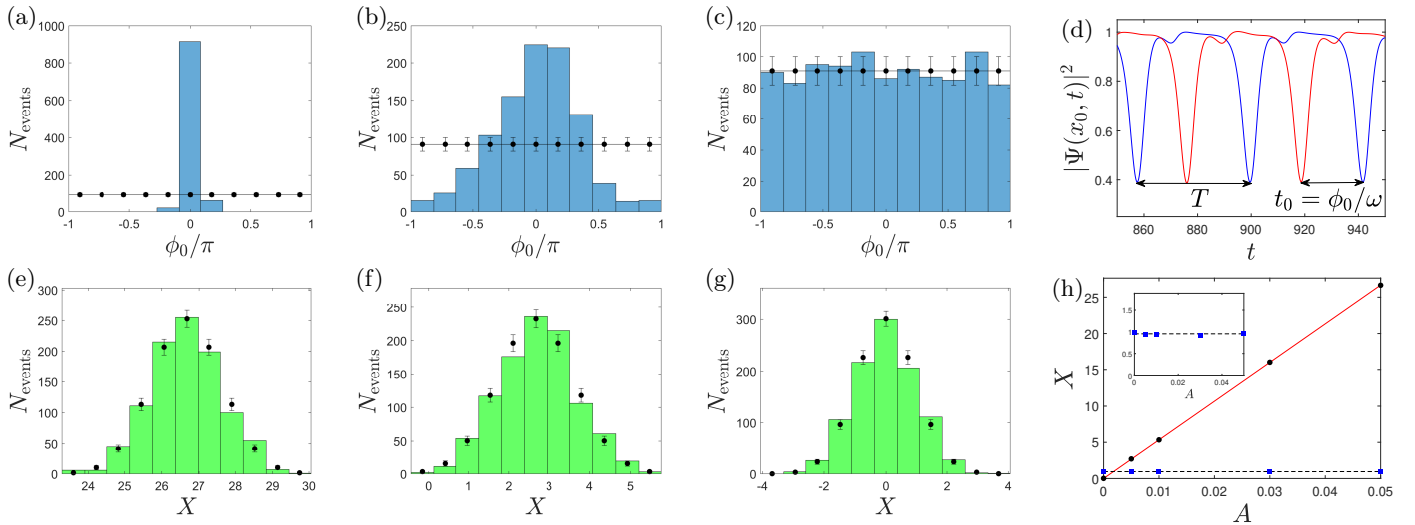


FIG. 3. (a)-(c) Histogram: phase-shift ϕ_0 for the TW ensembles of Figs. 2a-c. Horizontal line with error bars: uniform distribution and its statistical uncertainty. (d) Schematic obtention of ϕ_0 . Blue line: mean-field trajectory. Red line: particular TW realization. (e)-(g) Histogram: lasing amplitude X at $t = 0$ for (a)-(c). Dots with error bars: expected Gaussian distribution (8) and its statistical uncertainty. (h) Mean X_C (black dots) and statistical deviation ΔX_Q (blue squares) as a function of A , and their theoretical predictions (solid red and horizontal dashed black lines, respectively). Inset: Zoom of ΔX_Q .

spawning the anticorrelation bands [95]

$$\begin{aligned} \frac{x'}{v_u} - \frac{x}{v_d} &= \frac{x_u^{(0)}}{v_u} - \frac{x_d^{(0)}}{v_d} + \tau + nT, \quad n \in \mathbf{Z}, \\ \frac{x'}{v_w} - \frac{x}{v_d} &= \frac{x_w^{(0)}}{v_w} - \frac{x_d^{(0)}}{v_d} + \tau + nT, \quad n \in \mathbf{Z}. \end{aligned} \quad (7)$$

The remaining features are obtained by exchanging $x \longleftrightarrow x'$, $\tau \rightarrow -\tau$. Upper (lower) Eq. (7) is indicated by dashed magenta (white) lines in Figs. 2h-j, in good agreement with the observed patterns.

Remarkably, these anticorrelation bands are a nonlinear analogue of those arising from the spontaneous Andreev-Hawking effect [27], Fig. 2l (see Appendix). The celebrated Hawking moustache (magenta) and the Andreev band (white) result, respectively, from the anticorrelation of the normal Hawking (upstream, subsonic region) and copropagating (downstream, supersonic region) modes with the negative-energy downstream partner modes. In an HTC, the partner role is played by the soliton, synchronously emitted along with one wave upstream (Hawking) and another downstream (Andreev). Their correlation patterns become spatially periodic as a result of the HTC time-periodicity.

Time operators.— The spontaneous nature of the symmetry breaking is further revealed by the phase-shift distribution within the TW ensemble, Figs. 3a-c, obtained by examining the soliton passage in the late-time density $|\Psi(x_0, t)|^2$ at fixed $x = x_0 > 0$, Fig. 3d. As reference, we set $\phi_0 = 0$ for the mean-field wavefunction; for a purely quantum BHL, the mean-field reference is a simulation with $A = 0.003$. As expected, the distribution broad-

ens in the purely quantum limit, Fig. 3c, approaching a uniform distribution.

The late-time shifts are determined by the early-time shifts described by the DPA time operator, which only depends on the lasing amplitude \hat{X} (see Appendix). The TW histogram for X at $t = 0$ is shown in Figs. 3e-g, in excellent agreement with the expected Gaussian distribution (black dots with error bars):

$$W_0(X) = \frac{e^{-\frac{(X-X_C)^2}{2\Delta X_Q^2}}}{\sqrt{2\pi\Delta X_Q^2}}. \quad (8)$$

The mean $X_C \sim \sqrt{n_0}A$ is the coherent component of the lasing amplitude, while $\Delta X_Q \sim 1$ controls its quantum fluctuations; their values are shown in Fig. 3h as a function of A . Each lasing amplitude $X = X_C e^{-\Gamma t_0}$ is exponentially amplified as $X e^{\Gamma t}$, eventually yielding a CES state with oscillation phase-shift $\phi_0 = -\omega t_0$, so expectation values read

$$\langle O \rangle \simeq \int d\phi_0 W(\phi_0) O[\phi_0], \quad (9)$$

$$W(\phi_0) = \left| \frac{dX}{d\phi_0} \right| W_0(X), \quad \phi_0(X) = \frac{\omega}{\Gamma} \ln \frac{X}{X_C},$$

where $O[\phi_0]$ results from evaluating the observable O using $\hat{\Psi}(x, t) \simeq \Psi_0(x, \phi_0 + \omega t)$. Thus, $W(\phi_0)$ is the statistical distribution for the phase-shift operator $\hat{\phi}_0$, whose width $\Delta\phi_0$ is in turn controlled by ΔX_Q and ω/Γ . The HTC formation requires $\Delta\phi_0 \gtrsim 1$, which implies $\Delta X_Q \sim X_C$, $\omega/\Gamma \gtrsim 1$ [95]. Finite temperature and experimental noise do not spoil but rather strengthen the

phase-shift randomness as they increase $\Delta\phi_0$ [95]. Moreover, the time-crystalline nature of the HTC is further ensured by the underlying CES state, which is robust against perturbations and arises from a dynamical phase diagram [64].

Conclusions.—We formulate the concept of Hawking time crystal, i.e., a time crystal whose spontaneous symmetry breaking results from the self-amplification of spontaneous Hawking radiation. The HTC is signaled by time-independent expectation values for both the density and the ETCF, coexisting with a periodic OTCF. Interestingly, an HTC provides a nonlinear periodic analogue of the Andreev-Hawking effect, and its formation is understood using two different time operators. Although we focus on a particular model, the emergence of an HTC in a BHL is expected to be universal since its basic ingredients are quite general: strong lasing fluctuations and the long-time achievement of the CES state [59].

The formation of an HTC further demonstrates how analogue concepts can inspire applications in tabletop experiments, in addition to quantum amplifiers [63] or low-pass filters [106, 107]. Conversely, an HTC and the associated nonlinear Andreev-Hawking effect represent novel concepts in the analogue field, enhancing the intrinsic interest of a potential BHL realization. Our results can be translated into other systems governed by similar nonlinear equations of motion, such as magnonic condensates or nonlinear photonics [5, 10, 11, 108–110]. Another intriguing line of research is the characterization as quantum clocks [111, 112] of the two time operators here considered. From a broader perspective, any realization of time operator within a gravitational analogue scenario is of fundamental interest, since it provides a novel and tangible platform for foundational research on the quantum nature of time, including potential connections to quantum gravity.

This work has received funding from European Union’s Horizon 2020 research and innovation programme under the Marie Skłodowska-Curie Grant Agreement No. 847635, and from Spain’s Agencia Estatal de Investigación through Grant No. PID2022-139288NB-I00.

[1] W. G. Unruh, *Phys. Rev. Lett.* **46**, 1351 (1981).
[2] L. J. Garay, J. R. Anglin, J. I. Cirac, and P. Zoller, *Phys. Rev. Lett.* **85**, 4643 (2000).
[3] O. Lahav, A. Itah, A. Blumkin, C. Gordon, S. Rinott, A. Zayats, and J. Steinhauer, *Phys. Rev. Lett.* **105**, 240401 (2010).
[4] F. Belgiorno, S. L. Cacciatori, M. Clerici, V. Gorini, G. Ortenzi, L. Rizzi, E. Rubino, V. G. Sala, and D. Faccio, *Phys. Rev. Lett.* **105**, 203901 (2010).
[5] J. Drori, Y. Rosenberg, D. Bermúdez, Y. Silberberg, and U. Leonhardt, *Phys. Rev. Lett.* **122**, 010404 (2019).
[6] B. Horstmann, B. Reznik, S. Fagnocchi, and J. I. Cirac, *Phys. Rev. Lett.* **104**, 250403 (2010).
[7] M. Wittemer, F. Hakelberg, P. Kiefer, J.-P. Schröder, C. Fey, R. Schützhold, U. Warring, and T. Schaetz, *Phys. Rev. Lett.* **123**, 180502 (2019).
[8] S. Weinfurtner, E. W. Tedford, M. C. J. Penrice, W. G. Unruh, and G. A. Lawrence, *Phys. Rev. Lett.* **106**, 021302 (2011).
[9] L.-P. Euvé, F. Michel, R. Parentani, T. G. Philbin, and G. Rousseaux, *Phys. Rev. Lett.* **117**, 121301 (2016).
[10] I. Carusotto and C. Ciuti, *Rev. Mod. Phys.* **85**, 299 (2013).
[11] K. Falque, A. Delhom, Q. Glorieux, E. Giacobino, A. Bramati, and M. J. Jacquet, *Phys. Rev. Lett.* **135**, 023401 (2025).
[12] Y.-H. Shi, R.-Q. Yang, Z. Xiang, Z.-Y. Ge, H. Li, Y.-Y. Wang, K. Huang, Y. Tian, X. Song, D. Zheng, *et al.*, *Nature Communications* **14**, 3263 (2023).
[13] P. Švančara, P. Smaniotti, L. Solidoro, J. F. MacDonald, S. Patrick, R. Gregory, C. F. Barenghi, and S. Weinfurtner, *Nature* **628**, 66 (2024).
[14] J.-C. Jaskula, G. B. Partridge, M. Bonneau, R. Lopes, J. Ruaudel, D. Boiron, and C. I. Westbrook, *Phys. Rev. Lett.* **109**, 220401 (2012).
[15] C.-L. Hung, V. Gurarie, and C. Chin, *Science* **341**, 1213 (2013).
[16] T. Torres, S. Patrick, A. Coutant, M. Richartz, E. W. Tedford, and S. Weinfurtner, *Nature Physics* **13**, 833 (2017).
[17] S. Eckel, A. Kumar, T. Jacobson, I. B. Spielman, and G. K. Campbell, *Phys. Rev. X* **8**, 021021 (2018).
[18] J. Hu, L. Feng, Z. Zhang, and C. Chin, *Nature Physics* **15**, 785 (2019).
[19] T. Torres, S. Patrick, M. Richartz, and S. Weinfurtner, *Phys. Rev. Lett.* **125**, 011301 (2020).
[20] S. Patrick, H. Goodhew, C. Gooding, and S. Weinfurtner, *Phys. Rev. Lett.* **126**, 041105 (2021).
[21] J. Steinhauer, M. Abuzarli, T. Aladjidi, T. Bienaimé, C. Piekarski, W. Liu, E. Giacobino, A. Bramati, and Q. Glorieux, *Nat. Commun.* **13**, 2890 (2022).
[22] C. Viermann, M. Sparn, N. Liebster, M. Hans, E. Kath, Á. Parra-López, M. Tolosa-Simeón, N. Sánchez-Kuntz, T. Haas, H. Strobel, *et al.*, *Nature* **611**, 260 (2022).
[23] U. Leonhardt, T. Kiss, and P. Öhberg, *J. Opt. B: Quantum Semiclass. Opt.* **5**, S42 (2003).
[24] R. Balbinot, A. Fabbri, S. Fagnocchi, A. Recati, and I. Carusotto, *Phys. Rev. A* **78**, 21603 (2008).
[25] I. Carusotto, S. Fagnocchi, A. Recati, R. Balbinot, and A. Fabbri, *New J. Phys.* **10**, 103001 (2008).
[26] J. Macher and R. Parentani, *Phys. Rev. A* **80**, 43601 (2009).
[27] A. Recati, N. Pavloff, and I. Carusotto, *Phys. Rev. A* **80**, 43603 (2009).
[28] I. Zapata, M. Albert, R. Parentani, and F. Sols, *New J. Phys.* **13**, 63048 (2011).
[29] P. E. Larré, A. Recati, I. Carusotto, and N. Pavloff, *Phys. Rev. A* **85**, 13621 (2012).
[30] J. R. M. de Nova, F. Sols, and I. Zapata, *Phys. Rev. A* **89**, 043808 (2014).
[31] S. Finazzi and I. Carusotto, *Phys. Rev. A* **90**, 033607 (2014).
[32] X. Busch and R. Parentani, *Phys. Rev. D* **89**, 105024 (2014).
[33] J. R. M. de Nova, F. Sols, and I. Zapata, *New J. Phys.* **17**, 105003 (2015).

[34] F. Michel, R. Parentani, and R. Zegers, *Phys. Rev. D* **93**, 065039 (2016).

[35] M. Isoard, N. Milazzo, N. Pavloff, and O. Giraud, *Phys. Rev. A* **104**, 063302 (2021).

[36] C. C. H. Ribeiro, S.-S. Baak, and U. R. Fischer, *Phys. Rev. D* **105**, 124066 (2022).

[37] C. C. Holanda Ribeiro and U. R. Fischer, *Phys. Rev. D* **107**, L121502 (2023).

[38] G. Ciliberto, S. Emig, N. Pavloff, and M. Isoard, *Phys. Rev. A* **109**, 063325 (2024).

[39] J. Steinhauer, *Nature Physics* **12**, 959 (2016).

[40] J. R. M. de Nova, K. Golubkov, V. I. Kolobov, and J. Steinhauer, *Nature* **569**, 688 (2019).

[41] V. I. Kolobov, K. Golubkov, J. R. M. de Nova, and J. Steinhauer, *Nature Physics* **17**, 362 (2021).

[42] I. Zapata and F. Sols, *Phys. Rev. Lett.* **102**, 180405 (2009).

[43] W. Schleich, *Quantum Optics in Phase Space* (Wiley-VCH, Berlin, 2001).

[44] D. Walls and G. Milburn, *Quantum Optics*, Springer Study Edition (Springer Berlin, Heidelberg, 2008).

[45] J. R. M. de Nova, P. F. Palacios, P. A. Guerrero, I. Zapata, and F. Sols, *Comptes Rendus. Physique* **25**, 1 (2024).

[46] S. Corley and T. Jacobson, *Phys. Rev. D* **59**, 124011 (1999).

[47] U. Leonhardt, T. Kiss, and P. Öhberg, *Phys. Rev. A* **67**, 33602 (2003).

[48] C. Barceló, A. Cano, L. J. Garay, and G. Jannes, *Phys. Rev. D* **74**, 024008 (2006).

[49] P. Jain, A. S. Bradley, and C. Gardiner, *Phys. Rev. A* **76**, 23617 (2007).

[50] A. Coutant and R. Parentani, *Phys. Rev. D* **81**, 84042 (2010).

[51] S. Finazzi and R. Parentani, *New J. Phys.* **12**, 095015 (2010).

[52] D. Faccio, T. Arane, M. Lamperti, and U. Leonhardt, *Classical and Quantum Gravity* **29**, 224009 (2012).

[53] F. Michel and R. Parentani, *Phys. Rev. D* **88**, 125012 (2013).

[54] F. Michel and R. Parentani, *Phys. Rev. A* **91**, 053603 (2015).

[55] J. R. M. de Nova, S. Finazzi, and I. Carusotto, *Phys. Rev. A* **94**, 043616 (2016).

[56] C. Peloquin, L.-P. Euvé, T. Philbin, and G. Rousseaux, *Phys. Rev. D* **93**, 084032 (2016).

[57] D. Bermúdez and U. Leonhardt, *Classical and Quantum Gravity* **36**, 024001 (2018).

[58] R. Bürkle, A. Gaidoukov, and J. R. Anglin, *New Journal of Physics* **20**, 083020 (2018).

[59] J. R. M. de Nova, P. F. Palacios, I. Carusotto, and F. Sols, *New Journal of Physics* **23**, 023040 (2021).

[60] J. D. Rincón-Estrada and D. Bermúdez, *Annalen der Physik* **533**, 2000239 (2021).

[61] H. Katayama, *Scientific Reports* **11**, 19137 (2021).

[62] J. Steinhauer, *Phys. Rev. D* **106**, 102007 (2022).

[63] J. R. M. de Nova and F. Sols, *Phys. Rev. Res.* **5**, 043282 (2023).

[64] J. R. M. de Nova and F. Sols, *Phys. Rev. A* **105**, 043302 (2022).

[65] J. R. Muñoz de Nova and F. Sols, *Quantum* **9**, 1850 (2025).

[66] F. Wilczek, *Phys. Rev. Lett.* **109**, 160401 (2012).

[67] K. Sacha and J. Zakrzewski, *Reports on Progress in Physics* **81**, 016401 (2017).

[68] K. Sacha, *Time crystals* (Springer Cham, Switzerland, 2020).

[69] K. Sacha, *Phys. Rev. A* **91**, 033617 (2015).

[70] D. V. Else, B. Bauer, and C. Nayak, *Phys. Rev. Lett.* **117**, 090402 (2016).

[71] A. Pizzi, A. Nunnenkamp, and J. Knolle, *Phys. Rev. Lett.* **127**, 140602 (2021).

[72] B. Ye, F. Machado, and N. Y. Yao, *Phys. Rev. Lett.* **127**, 140603 (2021).

[73] D. Bhowmick, H. Sun, B. Yang, and P. Sengupta, *Phys. Rev. B* **108**, 014434 (2023).

[74] A. Syrid, J. Zakrzewski, and K. Sacha, *Phys. Rev. Lett.* **119**, 250602 (2017).

[75] F. Iemini, A. Russomanno, J. Keeling, M. Schirò, M. Dalmonte, and R. Fazio, *Phys. Rev. Lett.* **121**, 035301 (2018).

[76] B. Buća, J. Tindall, and D. Jaksch, *Nature Communications* **10**, 1730 (2019).

[77] C. Booker, B. Buća, and D. Jaksch, *New Journal of Physics* **22**, 085007 (2020).

[78] R. Daviet, C. P. Zelle, A. Rosch, and S. Diehl, *Phys. Rev. Lett.* **132**, 167102 (2024).

[79] S. Choi, J. Choi, R. Landig, G. Kucska, H. Zhou, J. Isoya, F. Jelezko, S. Onoda, H. Sumiya, V. Khemani, *et al.*, *Nature* **543**, 221 (2017).

[80] J. Zhang, P. Hess, A. Kyprianidis, P. Becker, A. Lee, J. Smith, G. Pagano, I.-D. Potirniche, A. C. Potter, A. Vishwanath, *et al.*, *Nature* **543**, 217 (2017).

[81] S. Autti, V. B. Eltsov, and G. E. Volovik, *Phys. Rev. Lett.* **120**, 215301 (2018).

[82] J. Smits, L. Liao, H. T. C. Stoof, and P. van der Straten, *Phys. Rev. Lett.* **121**, 185301 (2018).

[83] J. Rovny, R. L. Blum, and S. E. Barrett, *Phys. Rev. Lett.* **120**, 180603 (2018).

[84] A. Kyprianidis, F. Machado, W. Morong, P. Becker, K. S. Collins, D. V. Else, L. Feng, P. W. Hess, C. Nayak, G. Pagano, N. Y. Yao, and C. Monroe, *Science* **372**, 1192 (2021).

[85] J. Randall, C. E. Bradley, F. V. van der Gonden, A. Galicia, M. H. Abobeih, M. Markham, D. J. Twitchen, F. Machado, N. Y. Yao, and T. H. Taminiau, *Science* **374**, 1474 (2021).

[86] X. Mi, M. Ippoliti, C. Quintana, A. Greene, Z. Chen, J. Gross, F. Arute, K. Arya, J. Atalaya, R. Babbush, *et al.*, *Nature* **601**, 531 (2022).

[87] P. Frey and S. Rachel, *Science Advances* **8**, eabm7652 (2022).

[88] P. Kongkhambut, J. Skulte, L. Mathey, J. G. Cosme, A. Hemmerich, and H. Keßler, *Science* **377**, 670 (2022).

[89] D. Dreon, A. Baumgärtner, X. Li, S. Hertlein, T. Esslinger, and T. Donner, *Nature* **608**, 494 (2022).

[90] T. Liu, J.-Y. Ou, K. F. MacDonald, and N. I. Zheludev, *Nature Physics* **19**, 986 (2023).

[91] A. Greilich, N. E. Kopteva, A. N. Kamenskii, P. S. Sokolov, V. L. Korenev, and M. Bayer, *Nature Physics* **20**, 631 (2024).

[92] I. Carraro-Haddad, D. L. Chafatinos, A. Kuznetsov, I. A. Papuccio-Fernández, A. A. Reynoso, A. Bruchhausen, K. Biermann, P. Santos, G. Usaj, and A. Fainstein, *Science* **384**, 995 (2024).

[93] W. Wang, M. Feng, Q. Ma, Z. Cai, E. Li, and G. Liu, *Communications Physics* **8**, 191 (2025).

[94] C. Menotti and S. Stringari, *Phys. Rev. A* **66**, 043610 (2002).

[95] See Supplemental Material for technical details.

[96] M. Moeckel and S. Kehrein, *Phys. Rev. Lett.* **100**, 175702 (2008).

[97] B. Sciolla and G. Biroli, *Phys. Rev. Lett.* **105**, 220401 (2010).

[98] J. Lang, B. Frank, and J. C. Halimeh, *Phys. Rev. Lett.* **121**, 130603 (2018).

[99] I. Carusotto, S. X. Hu, L. A. Collins, and A. Smerzi, *Phys. Rev. Lett.* **97**, 260403 (2006).

[100] Y.-H. Wang, T. Jacobson, M. Edwards, and C. W. Clark, *Phys. Rev. A* **96**, 023616 (2017).

[101] Y.-H. Wang, T. Jacobson, M. Edwards, and C. W. Clark, *SciPost Phys.* **3**, 022 (2017).

[102] A. Sinatra, C. Lobo, and Y. Castin, *J. Phys. B: At. Mol. Opt. Phys.* **35**, 3599 (2002).

[103] M. Jacquet, M. Joly, F. Claude, L. Giacomelli, Q. Glorieux, A. Bramati, I. Carusotto, and E. Giacobino, *The European Physical Journal B* **76**, 152 (2022).

[104] S. Butera and I. Carusotto, *Phys. Rev. Lett.* **130**, 241501 (2023).

[105] H. Keßler, J. G. Cosme, M. Hemmerling, L. Mathey, and A. Hemmerich, *Phys. Rev. A* **99**, 053605 (2019).

[106] J. R. M. de Nova, D. Guéry-Odelin, F. Sols, and I. Zapata, *New J. Phys.* **16**, 123033 (2014).

[107] J. R. M. de Nova, F. Sols, and I. Zapata, *Annalen der Physik* **529**, 1600385 (2017).

[108] J. T. Mäkinen, S. Autti, and V. B. Eltsov, *Applied Physics Letters* **124**, 100502 (2024).

[109] P. D. Drummond and M. Hillery, *The quantum theory of nonlinear optics* (Cambridge University Press, 2014).

[110] H. S. Nguyen, D. Gerace, I. Carusotto, D. Sanvitto, E. Galopin, A. Lemaître, I. Sagnes, J. Bloch, and A. Amo, *Phys. Rev. Lett.* **114**, 036402 (2015).

[111] V. Singh, E. Kwon, and G. Milburn, [arXiv:2503.12118](https://arxiv.org/abs/2503.12118) (2025).

[112] L. Viotti, M. Huber, R. Fazio, and G. Manzano, [arXiv:2505.08276](https://arxiv.org/abs/2505.08276) (2025).

APPENDIX

FPBHL dynamics. The condensate dynamics for $t \geq 0$ in our FPBHL model is governed by the GP equation

$$i\partial_t \Psi(x, t) = \left[-\frac{1}{2}\partial_x^2 + g(x) [|\Psi(x, t)|^2 - 1] + 1 \right] \Psi(x, t),$$

$$g(x) = 1 + (c_2^2 - 1)\theta(x + L/2)\theta(L/2 - x). \quad (10)$$

For times $t < 0$ before the quench, $g(x) = 1$. Hence, $\Psi(x, t) = e^{i(vx - i\mu_0 t)}$, with $\mu_0 = 1 + v^2/2$, is a stationary GP solution at all times. However, the field fluctuations

$$\hat{\Psi}(x, t) = \left[1 + \frac{\hat{\varphi}(x, t)}{\sqrt{n_0}} \right] e^{i(vx - \mu_0 t)} \quad (11)$$

do experience nontrivial dynamics after the quench, described at the linear level by the Bogoliubov-de Gennes

(BdG) equations

$$i\partial_t \hat{\Phi} = M_0 \hat{\Phi}, \quad \hat{\Phi} = \begin{bmatrix} \hat{\varphi} \\ \hat{\varphi}^\dagger \end{bmatrix}, \quad (12)$$

$$M_0 = \begin{bmatrix} -\frac{1}{2}\partial_x^2 - iv\partial_x + g(x) & g(x) \\ -g(x) & \frac{1}{2}\partial_x^2 - iv\partial_x - g(x) \end{bmatrix}.$$

In general, BdG solutions can be expanded in terms of a complete set of eigenmodes $M_0 z_n = \omega_n z_n$, which are orthogonal under the inner product

$$(z_n | z_m) \equiv \int dx z_n^\dagger(x) \sigma_z z_m(x), \quad (13)$$

σ_z being the Pauli matrices. This is because M_0 is pseudo-Hermitian, i.e., $(z_n | M_0 z_m) = (M_0 z_n | z_m)$. Nevertheless, both M_0 and the inner product are not positive semidefinite; the conjugate mode $\bar{z}_n \equiv \sigma_x z_n^*$ satisfies $M_0 \bar{z}_n = -\omega_n^* \bar{z}_n$, $(z_n | z_m) = -(\bar{z}_m | \bar{z}_n)$.

For $t < 0$, M_0 is a homogeneous operator, diagonal in the Fourier basis:

$$M_0 z_k = \omega_k z_k, \quad z_k(x) = \frac{e^{ikx}}{\sqrt{L}} s_k, \quad (14)$$

$$s_k = \begin{bmatrix} u_k \\ v_k \end{bmatrix}, \quad u_k = \frac{\frac{k^2}{2} + (\omega_k - vk)}{\sqrt{2k^2|\omega_k - vk|}}, \quad v_k = \frac{\frac{k^2}{2} - (\omega_k - vk)}{\sqrt{2k^2|\omega_k - vk|}},$$

where the dispersion relation is

$$(\omega_k - vk)^2 = c^2 k^2 + \frac{k^4}{4}, \quad (15)$$

the speed of sound $c = \sqrt{g}$ being $c = 1$ in this case. The field spinor is expanded for $t < 0$ as

$$\hat{\Phi}(x, t) = \sum_k \hat{\alpha}_k z_k(x) e^{-i\omega_k t} + \hat{\alpha}_k^\dagger \bar{z}_k(x) e^{i\omega_k t}, \quad (16)$$

where $\hat{\alpha}_k$ is the annihilation operator associated to the mode z_k .

For $t \geq 0$, apart from the real spectrum of scattering states [51] (irrelevant for our discussion and neglected in the following), a dynamical instability emerges above critical velocities v_n such that [53]

$$L = \frac{2\pi n + \arctan \sqrt{\frac{1 - v_n^2}{v_n^2 - c_2^2}}}{2\sqrt{v_n^2 - c_2^2}}, \quad n = 0, 1, \dots \quad (17)$$

The n -th mode is degenerate for $v_n \leq v \leq v_{n+1/2}$, developing a non-vanishing real part of the frequency for $v > v_{n+1/2}$. In this work, we restrict to short cavities satisfying $v_0 < v < v_{1/2}$, so the FPBHL only displays a single, degenerate unstable mode, with purely imaginary frequency $\Omega = -\Omega^* \equiv i\Gamma$, $\Gamma > 0$. Specifically, there are two complex BdG modes, satisfying

$$M_0 z_I = \Omega z_I, \quad M_0 z_S = \Omega^* z_S, \quad z_{I,S} = \begin{bmatrix} u_{I,S} \\ v_{I,S} \end{bmatrix}. \quad (18)$$

It can be seen that one can choose both $z_I = \bar{z}_I$ and $z_S = \bar{z}_S$, satisfying the normalization condition $(z_I|z_S) = i$, with $(z_I|z_I) = (z_S|z_S) = 0$. Moreover, due to the even parity of $g(x)$, $g(x) = g(-x)$, the BdG equations are PT invariant, which implies that one can take $z_S(x) = -z_I^*(-x)$. Their contribution to the field spinor reads

$$\hat{\Phi}(x, t) \simeq \hat{X}z_I(x)e^{\Gamma t} + \hat{P}z_S(x)e^{-\Gamma t}, \quad (19)$$

since their quantum amplitudes precisely behave as conjugate position-momentum operators because

$$\hat{X} = i(z_S|\hat{\Phi}), \quad \hat{P} = -i(z_I|\hat{\Phi}) \implies [\hat{X}, \hat{P}] = (z_I|z_S) = i. \quad (20)$$

A proper annihilation operator is then constructed as

$$\hat{a} = \frac{\hat{X} + i\hat{P}}{\sqrt{2}}. \quad (21)$$

In terms of this mode, the BHL behaves as a DPA since, after neglecting c -number contributions, the grand-canonical Hamiltonian governing the BdG dynamics takes the form [45, 51]

$$\hat{K} = \hat{H} - \mu\hat{N} \simeq \hat{K}_{\text{DPA}} \equiv i\Gamma \frac{(\hat{a}^\dagger)^2 - \hat{a}^2}{2} = \Gamma \frac{\hat{X}\hat{P} + \hat{P}\hat{X}}{2}. \quad (22)$$

The density fluctuations in the BdG approximation read $\hat{\Psi}^\dagger(x, t)\hat{\Psi}(x, t) \simeq 1 + \delta\hat{n}(x, t)$, with

$$\delta\hat{n}(x, t) \equiv \frac{\hat{\varphi}(x, t) + \hat{\varphi}^\dagger(x, t)}{\sqrt{n_0}} = \frac{\hat{X}r_I(x)e^{\Gamma t} + \hat{P}r_S(x)e^{-\Gamma t}}{\sqrt{n_0}}, \quad (23)$$

$r_{I,S}(x) = u_{I,S}(x) + v_{I,S}(x) = 2\text{Re}[u_{I,S}(x)]$ being the corresponding density wavefunction; $\text{Re}[u_I(x)]$ is depicted in Fig. 1a in dashed-dotted green. The saturation regime is reached when $\delta\hat{n}(x, t) \sim 1$, i.e., $\hat{X}e^{\Gamma t} \sim \sqrt{n_0} \gg 1$.

HTC figure of merit. We compute the Fourier transform $g^{(2)}(k, k', t, t')$ of the OTCF $g^{(2)}(x, x', t, t')$ in the downstream-upstream quadrant ($x > 0, x' < 0$), which characterizes the Hawking-like correlations between the upstream wave and the downstream soliton. Due to their ballistic nature, we expect Fourier peaks in the upstream/downstream regions at $k_{u,d} = \omega/|v_{u,d}|$, respectively [95]. Thus, we take

$$\mathcal{G}(t, t') \equiv \frac{g^{(2)}(k_d, k_u, t, t')}{g_{\text{HTC}}^{(2)}(k_d, k_u, \tau = 0)}, \quad (24)$$

as figure of merit. The normalization is chosen such that the theoretical prediction is simply $\mathcal{G}_{\text{HTC}}(\tau) = e^{i\omega\tau}$ [95], which results from replacing the numerator above by $g_{\text{HTC}}^{(2)}(k_d, k_u, \tau)$, so $\mathcal{G}(\tau; t) \equiv \mathcal{G}(t, t + \tau) = \mathcal{G}_{\text{HTC}}(\tau)$.

Andreev-Hawking vs. HTC. The plot in Fig. 2l shows the ETCF at $t = 500$ for a TW simulation of a black hole, computed in the same way as for the FPPBHL case (10) but now $g(x) = 1 + (c_2^2 - 1)\theta(x)$ for $t \geq 0$, with

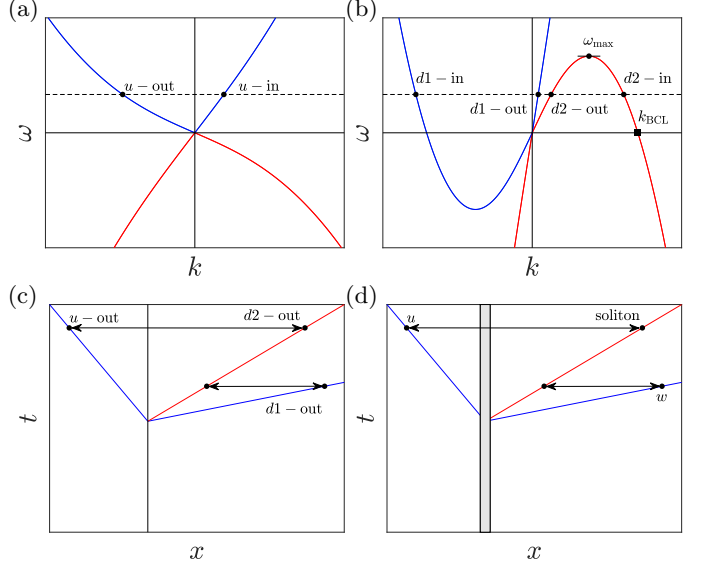


FIG. 4. (a)-(b) Schematic representation of the dispersion relation (15) for a subsonic ($c > v$) and supersonic ($c < v$) flow. (c) Spacetime diagram of the outgoing modes in an analogue black hole. Vertical line indicates the horizon at $x = 0$. (d) Same as (c) but for an HTC, where the vertical gray band now represents the finite lasing cavity.

$c_2 < v$. Thus, the upstream/downstream regions are subsonic/supersonic, with a dispersion relation schematically depicted in Figs. 4a-b, where “in” modes travel towards the horizon while “out” modes travel outwards the horizon, here exactly placed at $x = 0$. Blue line represents ω_k , Eq. (15), and red line is the conjugate $-\omega_{-k}$.

The Andreev-Hawking effect is characterized by the spontaneous, correlated emission of outgoing modes from the horizon (see spacetime diagram in Fig. 4c). Specifically, Hawking correlations involve the normal u -out (denoted as the Hawking mode in this context) and the anomalous $d2$ -out (partner) modes, while Andreev correlations involve the normal $d1$ -out (copropagating) and the anomalous $d2$ -out modes. This establishes a direct analogy with the traveling features of an HTC, whose spacetime diagram is shown in Fig. 4d. The nonlinear counterpart of the anomalous partner $d2$ modes are the solitons, carrying a density defect, while the upstream/downstream waves with positive amplitude are akin to the normal $u/d1$ modes. The role of the horizon (vertical black line in Fig. 4c) is here played by the localized lasing cavity (vertical gray band in Fig. 4d).

The Hawking moustache and the Andreev band in Fig. 2l are predicted using the long-wavelength hydrodynamic limit, where $\omega(k) \simeq v_i k$ with $v_u = v - 1$, $v_{d1,d2} = v \pm c_2$ [27]. Their trajectory is obtained by replacing $v_u \rightarrow v_u$, $v_w \rightarrow v_{d1}$, $v_d \rightarrow v_{d2}$, and setting $\tau = T = 0$ in Eq. (7), reinforcing the physical picture of the HTC as a nonlinear periodic analogue of the Andreev-Hawking effect. Dispersive effects also manifest similarly: i) in the HTC,

as yellow bands parallel to the dashed magenta lines in Figs. 2h-j, representing the positive correlation between the upstream wave and soliton minima (see magenta circles in Fig. 2d); ii) in the Andreev-Hawking effect, as parallel fringes to the main correlation bands in Fig. 2l.

Lasing and time-shift distributions. For $t < 0$, the quantum state is the quasiparticle vacuum $|0\rangle$, $\hat{\alpha}_k|0\rangle = 0$. The initial coherent perturbation is described as a classical contribution $\Phi_C(x) = [\delta\Psi_C \ \delta\Psi_C^*]^T$ to the initial field fluctuations:

$$\hat{\Phi}(x, 0) = \sqrt{n_0}A\Phi_C(x) + \sum_k \hat{\alpha}_k z_k(x) + \hat{\alpha}_k^\dagger \bar{z}_k(x). \quad (25)$$

The lasing amplitude at $t = 0$ then reads

$$\hat{X} = i(z_S|\hat{\Phi}(0)) = X_C + \frac{1}{\sqrt{L}} \sum_k \hat{\alpha}_k \beta_k + \hat{\alpha}_k^\dagger \beta_k^*. \quad (26)$$

Since the Wigner distribution for the quasiparticle amplitudes α_k is Gaussian, the initial Wigner distribution for X is also Gaussian, Eq. (8), determined by its mean

and variance [95]:

$$\langle \hat{X} \rangle = X_C \equiv i(z_S|\Phi_C)\sqrt{n_0}A, \quad (27)$$

$$\Delta X_Q^2 \equiv \langle \hat{X}^2 \rangle - \langle \hat{X} \rangle^2 = \frac{1}{L} \sum_k |\beta_k|^2 = \frac{1}{2\pi} \int dk |\beta_k|^2.$$

Thus, $\beta_k \equiv i\sqrt{L}(z_S|z_k)$ controls the quantum fluctuations of the lasing mode, in analogy to the usual Hawking coefficient β_ω [26].

For $t \geq 0$, the DPA dynamics (22) exponentially amplifies position eigenstates $(\hat{X}|X\rangle = X|X\rangle)$ as $e^{-i\hat{K}t}|X\rangle = e^{\frac{\Gamma t}{2}}|Xe^{\Gamma t}\rangle$. This allows to define a time operator by [95]

$$\hat{t} \equiv -\frac{1}{\Gamma} \ln \left| \frac{\hat{X}}{X_C} \right|, \quad [\hat{t}, \hat{K}] = -i. \quad (28)$$

Thus, the evolution of any lasing amplitude $X = X_C e^{-\Gamma t_0}$ is obtained by shifting the mean-field trajectory a time t_0 , yielding an asymptotic oscillation phase-shift

$$\phi_0(X) = -\omega t_0 = \frac{\omega}{\Gamma} \ln \frac{X}{X_C}. \quad (29)$$

This derivation assumes that X and X_C have the same sign, valid for weak-to-moderate quantum fluctuations. The case of arbitrary X is also understood in terms of the time operator in a similar fashion, with some technical corrections [95].

SUPPLEMENTAL MATERIAL

Lasing mode computation

We briefly sketch the computation of the frequency and wavefunction of the complex modes z_I, z_S . First, they can be determined from the time-independent Bogoliubov-de Gennes (BdG) equations (see Refs. [53, 54] for more details):

$$\begin{aligned} M_0 z_I &= \Omega z_I, \quad M_0 z_S = \Omega^* z_S, \quad z_{I,S} = \begin{bmatrix} u_{I,S} \\ v_{I,S} \end{bmatrix}, \\ M_0 &= \begin{bmatrix} -\frac{1}{2}\partial_x^2 - iv\partial_x + g(x) & g(x) \\ -g(x) & \frac{1}{2}\partial_x^2 - iv\partial_x - g(x) \end{bmatrix}, \quad g(x) = 1 + (c_2^2 - 1)\theta(x + L/2)\theta(L/2 - x), \end{aligned} \quad (30)$$

with $\text{Im } \Omega > 0$. Since the problem is piecewise homogeneous, it can be solved by matching the different plane waves in each homogeneous region, which now have complex wavevectors, given by the zeros of the polynomial equation

$$(\Omega - vk)^2 = c^2 k^2 + \frac{k^4}{4}, \quad (31)$$

where c is the corresponding speed of sound. The BdG plane-wave solutions associated to each wavevector read

$$M_0 z_k = \Omega z_k, \quad z_k(x) = e^{ikx} \begin{bmatrix} \frac{k^2}{2} + (\Omega - vk) \\ \frac{k^2}{2} - (\Omega - vk) \end{bmatrix}. \quad (32)$$

Notice that we skip here normalization factors since these are non-normalizable solutions with complex wavevector. Specifically, inside the lasing cavity, $|x| < L/2$, we have 4 complex modes while, in each asymptotic subsonic region, $|x| > L/2$, we only have 2 asymptotically bounded modes. Hence, in total, we have 8 degrees of freedom, corresponding

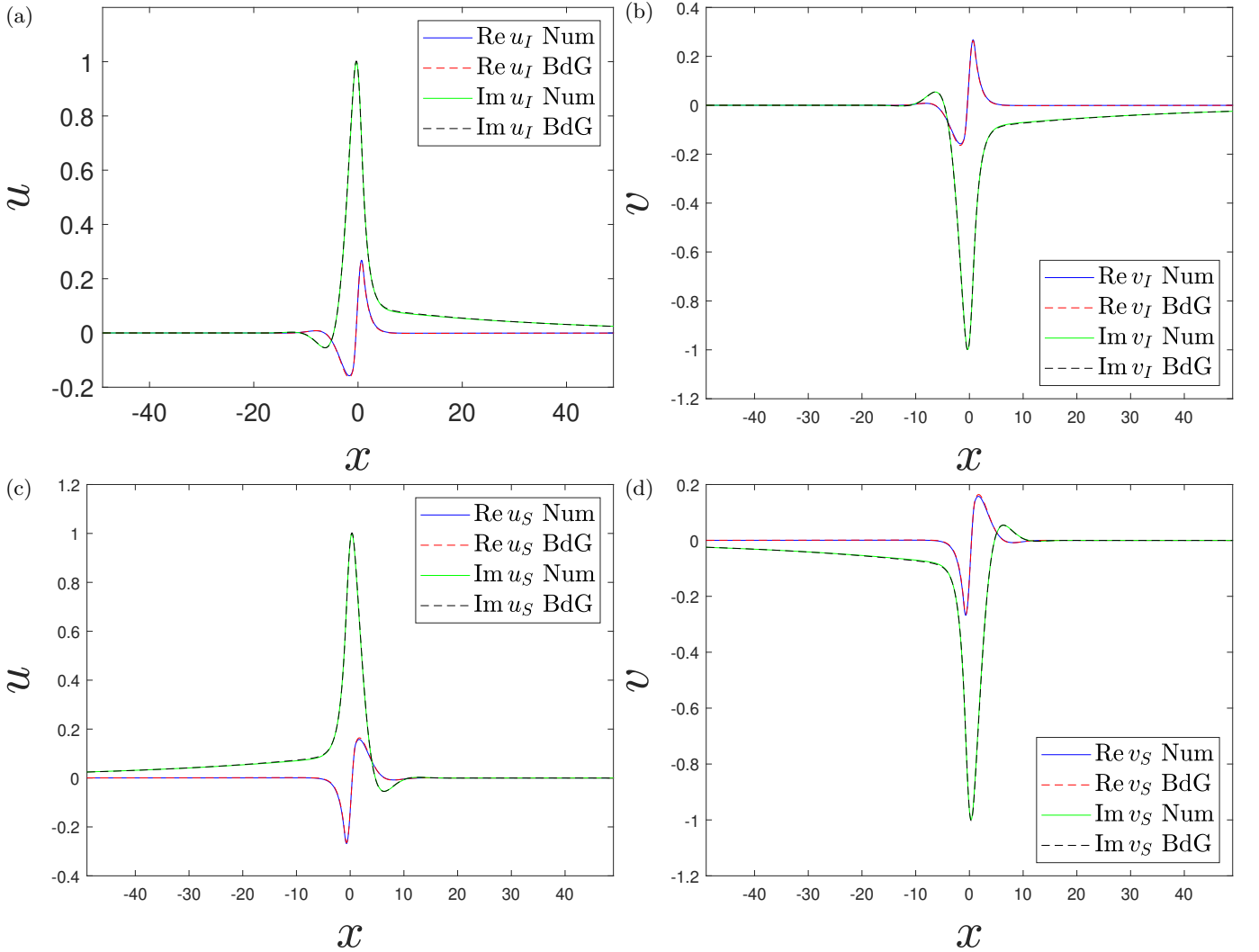


FIG. 5. (a)-(d) Spatial profile of the real and imaginary part of the BdG components u_I, v_I, u_S, v_S , respectively. Solid lines are numerically obtained by finite methods and dashed lines are the analytical result from solving the BdG scattering problem [see Eq. (33) and ensuing discussion].

to the amplitude of each of these modes. On the other hand, each matching at $x = \pm L/2$ imposes 4 equations (2 for z_I and 2 for its derivative) so we have 8 linear equations for 8 degrees of freedom. Thus, in order to display nontrivial solutions, the 8×8 matrix $A(\Omega)$ describing the homogeneous linear system of equations must satisfy

$$\det A(\Omega) = 0. \quad (33)$$

The zeros of this equation yield the complex frequencies Ω of the lasing modes. The same process is repeated for Ω^* , using the corresponding asymptotically bounded modes. Once obtained, the BdG spinors z_I, z_S are determined up to a global normalization factor, which is fixed by the conditions

$$z_I = \bar{z}_I, \quad z_S = \bar{z}_S, \quad (z_I|z_S) = i, \quad (34)$$

and by $z_S(x) = -z_I^*(-x)$, where this latter relation is a specific feature of the FPBHL, resulting from its PT invariance.

Alternatively, we have found here that Ω, Ω^* and z_I, z_S can be simply obtained by numerically diagonalizing the BdG operator M_0 using finite methods. A very good agreement is observed between both techniques, Fig. 5, where the expected relations $u_I(x) = v_I^*(x) = -u_S^*(-x) = -v_S(-x)$ can be also seen.

Truncated Wigner method

The Truncated Wigner (TW) method computes symmetric-ordered expectation values from ensemble averages of integrations of the Gross-Pitaevskii (GP) equation [25, 102], which here reads

$$i\partial_t \Psi_W(x, t) = \left[-\frac{1}{2}\partial_x^2 + g(x) [|\Psi_W(x, t)|^2 - 1] + 1 \right] \Psi_W(x, t), \quad (35)$$

by using a stochastic initial condition

$$\Psi_W(x, 0) = \left[1 + A\delta\Psi_C(x) + \frac{\varphi_W(x)}{\sqrt{n_0}} \right] e^{ivx} \equiv \left[1 + \frac{\delta\Psi_W(x)}{\sqrt{n_0}} \right] e^{ivx}, \quad \delta\Psi_W(x) = \sqrt{n_0}A\delta\Psi_C(x) + \varphi_W(x), \quad (36)$$

where we absorb the initial classical stimulation $A\delta\Psi_C(x) = A \cos(\pi x/L) \theta(x + L/2) \theta(L/2 - x)$ within the lasing cavity into the definition of the field fluctuations. In turn, $\varphi_W(x)$ is expressed in terms of the BdG modes of the initial homogeneous condensate as

$$\begin{bmatrix} \varphi_W \\ \varphi_W^* \end{bmatrix} = \frac{1}{\sqrt{L}} \sum_k \alpha_k s_k e^{ikx} + \alpha_k^* \bar{s}_k e^{-ikx} = \sum_k \alpha_k z_k(x) + \alpha_k^* \bar{z}_k(x), \quad (37)$$

the amplitudes α_k, α_k^* being here stochastic variables distributed according to the Wigner function of the initial state. Specifically, we make the usual assumption that the initial quantum state is a thermal state at temperature $T = 1/\beta$ ($k_B = 1$) in the comoving frame of the condensate [26, 32]:

$$\hat{\rho} = \frac{e^{-\beta\hat{K}_C}}{Z}, \quad Z = \text{Tr } e^{-\beta\hat{K}_C}, \quad \hat{K}_C = \sum_k \Omega_k \hat{\alpha}_k^\dagger \hat{\alpha}_k. \quad (38)$$

The associated Wigner function is a Gaussian distribution characterized by the first and second-order momenta

$$\begin{aligned} \langle \alpha_k \rangle &= \langle \hat{\alpha}_k \rangle = 0, \quad \langle \alpha_{k'} \alpha_k \rangle = \langle \hat{\alpha}_{k'} \hat{\alpha}_k \rangle = 0, \\ \langle \alpha_{k'}^* \alpha_k \rangle &= \frac{\langle \hat{\alpha}_{k'}^\dagger \hat{\alpha}_k + \hat{\alpha}_k \hat{\alpha}_{k'}^\dagger \rangle}{2} = \left(n_k + \frac{1}{2} \right) \delta_{kk'} = \frac{\coth \frac{\beta \Omega_k}{2}}{2} \delta_{kk'}, \quad n_k = \frac{1}{e^{\beta \Omega_k} - 1}. \end{aligned} \quad (39)$$

By subtracting the constant factor $\delta_{kk'}/2$ in the last line, arising from the commutator between annihilation and creation operators, one retrieves the more usual normal-ordered expectation value $\langle \hat{\alpha}_{k'}^\dagger \hat{\alpha}_k \rangle$. The zero-temperature case considered in the main text amounts to setting $n_k = 0$,

$$\langle \alpha_{k'}^* \alpha_k \rangle = \frac{\delta_{kk'}}{2}. \quad (40)$$

For the TW simulations, we take the total length of the grid and particle number to be $L_t \approx 1885$ and $N = 10^8$, with $n_0 = N/L_t \approx 5.31 \times 10^4 \gg 1$ the condensate density. The number of modes included in the initial condition is $N_m = 3000 \ll N$, which corresponds to implement a momentum cutoff $|k| < k_C = 5$. Expectation values are evaluated after ensembles of 1000 simulations. The numerical method employed to integrate the GP equation is explained in detail in Ref. [55].

Technically, one should use a number-conserving approximation in the computations, taking the number of particles in the condensate as $N_0 = N - N_{\text{NC}}$, with N_{NC} the number of non-condensed particles

$$N_{\text{NC}} = \sum_k (|u_k|^2 + |v_k|^2) \langle \hat{\alpha}_k^\dagger \hat{\alpha}_k \rangle + |v_k|^2 = \sum_k (|u_k|^2 + |v_k|^2) \left(|\alpha_k|^2 - \frac{1}{2} \right) + |v_k|^2 \quad (41)$$

This is translated into a modified version of Eq. (36),

$$\Psi_W(x, 0) = \left[\sqrt{1 - \frac{N_{\text{NC}}}{N}} + \frac{\delta\Psi_W(x)}{\sqrt{n_0}} \right] e^{ivx}. \quad (42)$$

For the parameters considered, we have not found any significant effect resulting from the use of a non-conserving approximation.

Regarding the evaluation of observables, since averages over the TW ensemble are equivalent to symmetric-ordered expectation values, commutators of the form

$$[\hat{\Psi}(x, t), \hat{\Psi}^\dagger(x', t)] = \frac{1}{2\pi n_0} \int_{-k_C}^{k_C} dk e^{ik(x-x')} = \frac{\sin k_C(x-x')}{\pi n_0(x-x')} \quad (43)$$

arise in the symmetrization of observables evaluated at equal times, such as the density or the ETCF (the factor n_0^{-1} results from our unit convention). However, their contribution becomes negligible when compared to that from the time operator at late times. Similarly, regarding the OTCF, we will face commutators of the form $[\hat{\Psi}(x, t), \hat{\Psi}^\dagger(x', t')] \sim n_0^{-1} \ll 1$, which are once more negligible when compared to the late time-shift fluctuations. As a result of neglecting these commutators, expectation values can be simply evaluated at late times by taking averages over the TW ensemble with the substitution $\hat{\Psi}(x, t) \rightarrow \Psi_W(x, t)$ and $\hat{\Psi}^\dagger(x, t) \rightarrow \Psi_W^*(x, t)$.

Quantum distributions

We further explain the theoretical model used for the quantum distributions of the initial lasing amplitude X and the asymptotic phase-shift ϕ_0 , as well as their connection through their corresponding time operators.

Initial state: Lasing distribution

From the complex modes z_I, z_S , we construct a properly normalized mode

$$z = \frac{z_I - iz_S}{\sqrt{2}} \implies (z|z) = 1, \quad (44)$$

whose quantum amplitude is

$$(z|\hat{\Phi}) = \frac{\hat{X} + i\hat{P}}{\sqrt{2}} = \hat{a}, \quad (\bar{z}|\hat{\Phi}) = -\hat{a}^\dagger. \quad (45)$$

The inverse relations read:

$$\begin{aligned} z_I &= \frac{z + \bar{z}}{\sqrt{2}}, \quad z_S = i \frac{z - \bar{z}}{\sqrt{2}}, \\ \hat{X} &= \frac{\hat{a} + \hat{a}^\dagger}{\sqrt{2}}, \quad \hat{P} = -i \frac{\hat{a} - \hat{a}^\dagger}{\sqrt{2}}. \end{aligned} \quad (46)$$

By expanding the field spinor at $t = 0$ in terms of the quasiparticle modes and the classical field contribution as in Eq. (25) of the main text,

$$\hat{\Phi}(x, 0) = \sqrt{n_0} A \Phi_C(x) + \sum_k \hat{a}_k z_k(x) + \hat{a}_k^\dagger \bar{z}_k(x), \quad (47)$$

we find that

$$\begin{aligned} \hat{a} &= (z|\hat{\Phi}(0)) = \alpha_C + \frac{1}{\sqrt{L}} \sum_k c_k \hat{a}_k + d_k \hat{a}_k^\dagger, \\ \alpha_C &= (z|\Phi_C) \sqrt{n_0} A, \quad c_k = \sqrt{L}(z|z_k), \quad d_k = \sqrt{L}(z|\bar{z}_k). \end{aligned} \quad (48)$$

Using this expansion, we compute the initial Wigner function characterizing the distribution of the complex amplitude α associated to the annihilation operator \hat{a} at $t = 0$,

$$W_0(\alpha) = \int \frac{d^2\eta}{\pi^2} e^{\eta^* \alpha - \eta \alpha^*} \langle e^{\eta \hat{a}^\dagger - \eta^* \hat{a}} \rangle = \frac{2}{\pi} \frac{e^{-2 \frac{\lambda |\alpha - \alpha_C|^2 - \Delta^* (\alpha - \alpha_C)^2 - \Delta (\alpha^* - \alpha_C^*)^2}{\lambda^2 - 4|\Delta|^2}}}{\sqrt{\lambda^2 - 4|\Delta|^2}}, \quad (49)$$

where the expectation value is evaluated here using the thermal state (38), $\langle e^{\eta\hat{a}^\dagger - \eta^*\hat{a}} \rangle = \text{Tr}[e^{\eta\hat{a}^\dagger - \eta^*\hat{a}} \hat{\rho}]$, and

$$\begin{aligned}\lambda &\equiv \frac{1}{L} \sum_k (|c_k|^2 + |d_k|^2) \coth \frac{\beta\Omega_k}{2} = \frac{1}{2\pi} \int dk (|c_k|^2 + |d_k|^2) \coth \frac{\beta\Omega_k}{2}, \\ \Delta &= \Delta_x + i\Delta_y \equiv \frac{1}{L} \sum_k c_k d_k \coth \frac{\beta\Omega_k}{2} = \frac{1}{2\pi} \int dk c_k d_k \coth \frac{\beta\Omega_k}{2}.\end{aligned}\quad (50)$$

In terms of phase-space operators, from Eqs. (46)-(48), we find

$$\begin{aligned}\hat{X} &= i(z_S|\hat{\Phi}(0)) = X_C + \frac{1}{\sqrt{L}} \sum_k \beta_k \hat{a}_k + \beta_k^* \hat{a}_k^\dagger, \quad X_C = i(z_S|\Phi_C) \sqrt{n_0} A = \frac{\alpha_C + \alpha_C^*}{\sqrt{2}}, \quad \beta_k = i\sqrt{L}(z_S|z_k) = \frac{c_k + d_k^*}{\sqrt{2}}, \\ \hat{P} &= -i(z_I|\hat{\Phi}(0)) = P_C + \frac{1}{\sqrt{L}} \sum_k \delta_k \hat{a}_k + \delta_k^* \hat{a}_k^\dagger, \quad P_C = -i(z_I|\Phi_C) \sqrt{n_0} A = -i\frac{\alpha_C - \alpha_C^*}{\sqrt{2}}, \quad \delta_k = -i\sqrt{L}(z_I|z_k) = -i\frac{c_k - d_k^*}{\sqrt{2}}.\end{aligned}\quad (51)$$

Regarding their Wigner distribution, by rewriting α in terms of the phase-space variables X, P ,

$$\alpha = \frac{X + iP}{\sqrt{2}}, \quad (52)$$

we get, after proper normalization and employing compact matrix notation,

$$W_0(X, P) = \frac{\sqrt{\det M}}{2\pi} e^{-\frac{1}{2}(\mathbf{X} - \mathbf{X}_C)^\text{T} M(\mathbf{X} - \mathbf{X}_C)}, \quad \mathbf{X} = \begin{bmatrix} X \\ P \end{bmatrix}, \quad \mathbf{X}_C = \begin{bmatrix} X_C \\ P_C \end{bmatrix}, \quad M = \frac{2}{\lambda^2 - 4|\Delta|^2} \begin{bmatrix} \lambda - 2\Delta_x & -2\Delta_y \\ -2\Delta_y & \lambda + 2\Delta_x \end{bmatrix}. \quad (53)$$

From the usual Gaussian theory, we have that $\langle X \rangle = X_C$ and $\langle P \rangle = P_C$, while the second-order momenta involving the uncertainties $\Delta X = X - \langle X \rangle$ and $\Delta P = P - \langle P \rangle$ are obtained from the correlation matrix

$$C = \begin{bmatrix} \langle \Delta X^2 \rangle & \langle \Delta X \Delta P \rangle \\ \langle \Delta P \Delta X \rangle & \langle \Delta P^2 \rangle \end{bmatrix} = M^{-1} = \begin{bmatrix} \frac{\lambda}{2} + \Delta_x & \Delta_y \\ \Delta_y & \frac{\lambda}{2} - \Delta_x \end{bmatrix}. \quad (54)$$

Notice that $W_0(X, P)$ can be also derived directly from Eq. (51) after noticing Gaussianity, since any Gaussian distribution is determined by its first ($\langle X \rangle = \langle \hat{X} \rangle = X_C$, $\langle P \rangle = \langle \hat{P} \rangle = P_C$) and second-order momenta,

$$\begin{aligned}\langle \Delta X^2 \rangle &= \langle \hat{X}^2 \rangle - \langle \hat{X} \rangle^2 = \frac{1}{2\pi} \int dk |\beta_k|^2 \coth \frac{\beta\Omega_k}{2} = \frac{\lambda}{2} + \Delta_x, \\ \langle \Delta P^2 \rangle &= \langle \hat{P}^2 \rangle - \langle \hat{P} \rangle^2 = \frac{1}{2\pi} \int dk |\delta_k|^2 \coth \frac{\beta\Omega_k}{2} = \frac{\lambda}{2} - \Delta_x, \\ \langle \Delta X \Delta P \rangle &= \frac{\langle \hat{X} \hat{P} + \hat{P} \hat{X} \rangle}{2} - \langle \hat{X} \rangle \langle \hat{P} \rangle = \frac{1}{2\pi} \int dk \frac{\beta_k \delta_k^* + \beta_k^* \delta_k}{2} \coth \frac{\beta\Omega_k}{2} = \Delta_y.\end{aligned}\quad (55)$$

The marginal position, momentum distributions are also Gaussian,

$$W_0(X) = \frac{e^{-\frac{(X-X_C)^2}{2\Delta X^2}}}{\sqrt{2\pi\Delta X^2}}, \quad W_0(P) = \frac{e^{-\frac{(P-P_C)^2}{2\Delta P^2}}}{\sqrt{2\pi\Delta P^2}}, \quad (56)$$

where, hereafter, for the sake of simplicity, we denote $\Delta X^2 = \langle \Delta X^2 \rangle$ and $\Delta P^2 = \langle \Delta P^2 \rangle$.

Focusing on the lasing amplitude X , we separate pure quantum vacuum fluctuations from thermal fluctuations as

$$\Delta X^2 = \frac{1}{2\pi} \int dk |\beta_k|^2 \coth \frac{\beta\Omega_k}{2} = \frac{1}{2\pi} \int dk |\beta_k|^2 + \frac{1}{2\pi} \int dk |\beta_k|^2 \frac{2}{e^{\beta\Omega_k} - 1} \equiv \Delta X_Q^2 + \Delta X_T^2. \quad (57)$$

In the main text, we work at zero temperature, so only quantum fluctuations contribute, $\Delta X^2 = \Delta X_Q^2$. We represent $|\bar{\beta}_k|^2 \equiv |\beta_k|^2 \coth \frac{\beta\Omega_k}{2}$ in Fig. 6a for different temperatures $T = 0, 0.1, 0.5$. As it is clearly seen, $|\bar{\beta}_k|^2 \simeq 0$ for wavevectors above our cutoff $k_C = 5$.

The TW histograms for the distribution of X shown in the main text are numerically computed using the initial TW condition, Eqs. (36), (37):

$$X = i(z_S|\Phi_W) = X_C + \frac{1}{\sqrt{L}} \sum_k \alpha_k \beta_k + \alpha_k^* \beta_k^*, \quad \Phi_W = \begin{bmatrix} \delta\Psi_W \\ \delta\Psi_W^* \end{bmatrix}. \quad (58)$$

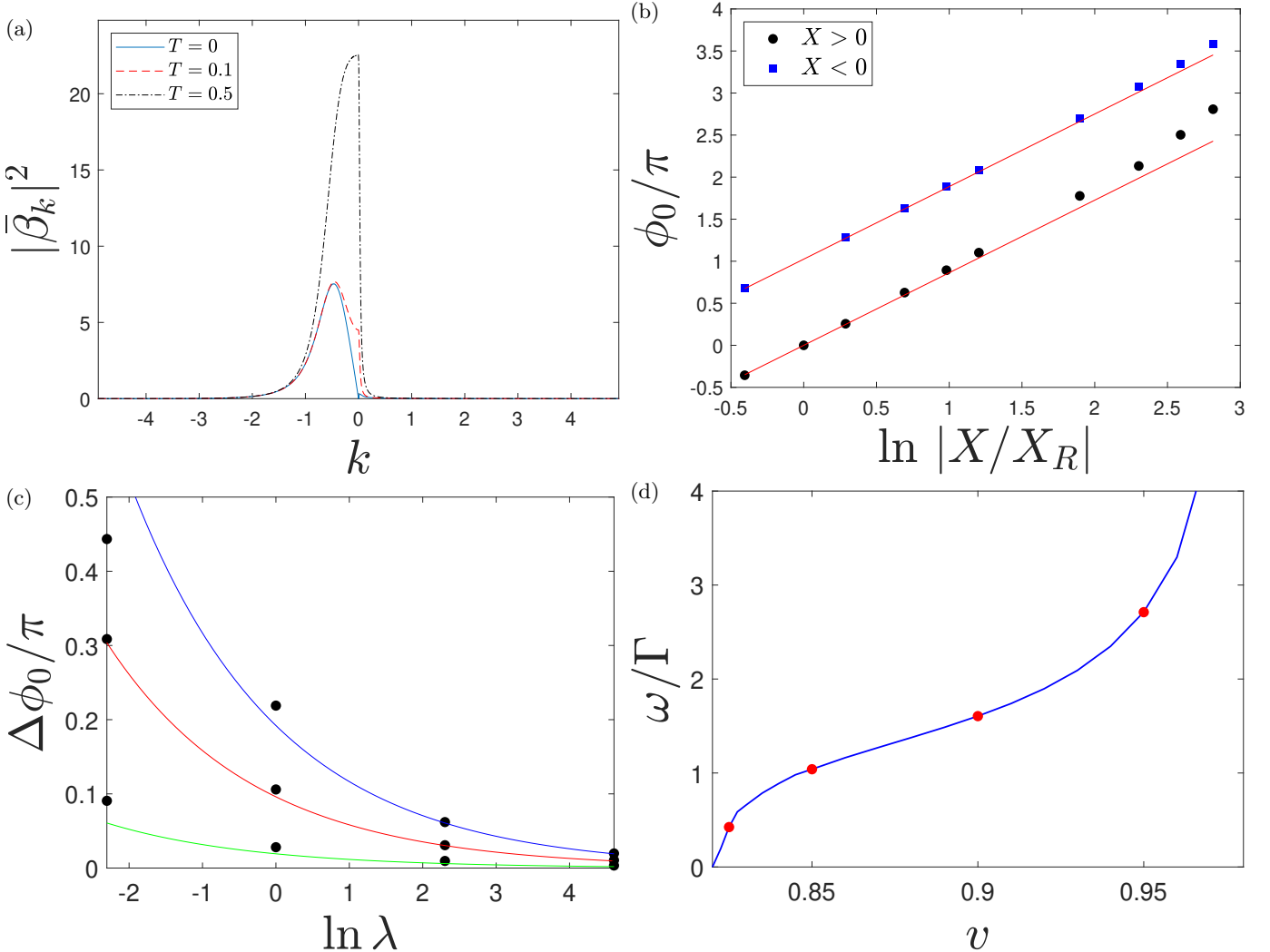


FIG. 6. (a) The coefficient $|\bar{\beta}_k|^2 \equiv |\beta_k|^2 \coth \frac{\beta \Omega_k}{2}$ as a function of k for $T = 0$ (solid blue), $T = 0.1$ (dashed red) and $T = 0.5$ (dashed-dotted black). The background FPBHL parameters are $v = 0.95, c_2 = 0.4, L = 2$. (b) Asymptotic phase-shift ϕ_0 as a function of the initial lasing amplitude X for both $X > 0$ (black dots) and $X < 0$ (blue squares). Red lines represent the theoretical prediction from Eq. (77), where the reference amplitude is $X_R \approx 1.60$, corresponding to an initial classical amplitude $A = 0.003$. The background FPBHL parameters are the same as in (a). (c) Phase-shift width $\Delta\phi_0$ as a function of the dimensionless parameter λ for $A = 0.005, 0.01, 0.5$ (black dots). Solid blue, red, green lines show the corresponding theoretical prediction from Eq. (79). The background FPBHL parameters are $v = 0.90, c_2 = 0.4, L = 2$. (d) ω/Γ as a function of the initial flow velocity v in the range $0.82 \approx v_c < v < v_{1/2} \approx 0.98$ for fixed $c_2 = 0.4, L = 2$.

Early times: Time operator in a degenerate parametric amplifier

Regarding dynamics, as explained in the main text, at early times when the BdG approximation is still valid, the time evolution of the lasing mode is governed by the grand-canonical Hamiltonian

$$\hat{K} \simeq \hat{K}_{\text{DPA}} \equiv i\Gamma \frac{(\hat{a}^\dagger)^2 - \hat{a}^2}{2} = \Gamma \frac{\hat{X}\hat{P} + \hat{P}\hat{X}}{2}, \quad (59)$$

giving rise to the time-evolution operator $U(t) = e^{-i\hat{K}t} = S(-\Gamma t)$, with $S(\varepsilon) = e^{\frac{\varepsilon^* \hat{a}^2 - \varepsilon (\hat{a}^\dagger)^2}{2}}$ the usual squeezing operator. Thus, remarkably, a degenerate lasing mode represents a textbook realization of a degenerate parametric amplifier (DPA).

In the Schrödinger picture, the eigenstates forming the continuous spectrum of the phase-space operators, $\hat{X}|X\rangle =$

$X|X\rangle$ and $\hat{P}|P\rangle = P|P\rangle$, are squeezed as

$$U(t)|X\rangle = e^{\frac{\Gamma t}{2}}|Xe^{\Gamma t}\rangle, \quad U(t)|P\rangle = e^{-\frac{\Gamma t}{2}}|Pe^{-\Gamma t}\rangle, \quad (60)$$

while the quantum state of the system evolves as $\hat{\rho}(t) = U(t)\hat{\rho}U^\dagger(t)$. In the Heisenberg picture, operators evolve as $O(t) = U^\dagger(t)OU(t)$, resulting in

$$\hat{a}(t) = \hat{a} \cosh \Gamma t + \hat{a}^\dagger \sinh \Gamma t, \quad \hat{X}(t) = \hat{X} e^{\Gamma t}, \quad \hat{P}(t) = \hat{P} e^{-\Gamma t}. \quad (61)$$

It is easy to show that this time evolution is translated into a time-dependent Wigner function

$$W(\alpha, t) = W_0(\alpha(t)) = W_0(\alpha \cosh \Gamma t - \alpha^* \sinh \Gamma t). \quad (62)$$

In terms of phase-space variables, this reads as

$$W(X, P, t) = W_0(X e^{-\Gamma t}, P e^{\Gamma t}). \quad (63)$$

As a result, the marginal distribution of the lasing amplitude $W(X, t) = e^{-\Gamma t} W_0(X e^{-\Gamma t})$ is also Gaussian, with exponentially increasing mean $X_C(t) = X_C e^{\Gamma t}$ and width $\Delta X(t) = \Delta X e^{\Gamma t}$.

We note that the vacuum $|0\rangle$ associated to the operator \hat{a} is not the true vacuum of \hat{K} , in the sense that any squeezed vacuum of the family $|r\rangle \equiv S(-r)|0\rangle$, $r \in \mathbb{R}$, is another valid choice since $S(r)\hat{K}S(-r) = \hat{K}$. Actually, \hat{K} has no normalizable eigenstates, and $|r = \Gamma t\rangle$ is just the result of evolving $|0\rangle$ in time as $|\Gamma t\rangle = U(t)|0\rangle$. Consequently, the choice of a specific instantaneous vacuum at a given time can be regarded as another form of spontaneous symmetry breaking, induced by the quantization process [36]. Nonetheless, this vacuum ambiguity is broken in our work by the presence of a well-defined initial state at $t = 0$.

This conceptual connection permits us to define a time operator for a DPA in terms of the position operator as

$$\hat{t} \equiv -\frac{1}{\Gamma} \ln \left| \frac{\hat{X}}{X_R} \right|, \quad (64)$$

with X_R some reference amplitude. The operator \hat{t} acts on any state $|\Psi\rangle$ in position representation, $\Psi(X) = \langle X|\Psi\rangle$, as

$$\langle X|\hat{t}|\Psi\rangle = -\frac{1}{\Gamma} \ln \left| \frac{X}{X_R} \right| \langle X|\Psi\rangle = -\frac{1}{\Gamma} \ln \left| \frac{X}{X_R} \right| \Psi(X). \quad (65)$$

By using this representation, and the fact that the momentum behaves as the usual differential operator $\langle X|\hat{P}|\Psi\rangle = -i\partial_X \Psi(X)$, it is immediate to show that \hat{t} satisfies the expected commutation relation for a time operator (notice that \hat{K} here plays the role of the Hamiltonian, generating the time evolution):

$$[\hat{t}, \hat{K}] = -i. \quad (66)$$

The spectrum of \hat{t} is continuous and degenerate, $\hat{t}|t\rangle_\pm = t|t\rangle_\pm$, presenting two branches labeled as \pm ,

$$|t\rangle_\pm \equiv \sqrt{\left| \frac{dX_\pm}{dt} \right|} |X_\pm(t)\rangle, \quad \hat{X}|X_\pm(t)\rangle = X_\pm(t)|X_\pm(t)\rangle, \quad X_\pm(t) = \pm|X_R|e^{-\Gamma t}. \quad (67)$$

The \pm branches result from considering the time involution (i.e., the time-reversed evolution) of positive/negative position eigenstates, respectively, which are not connected between them through the amplification dynamics. Therefore, physically, the time operator measures the time needed for a given lasing amplitude X to reach the reference values $\pm|X_R|$, which then fix a time origin. Different choices of X_R amount to choose different time origins.

These eigenstates form a complete

$$\sum_{a=\pm} \int_{-\infty}^{\infty} dt |t\rangle_a a\langle t| = \int_0^{\infty} dX |X\rangle \langle X| + \int_{-\infty}^0 dX |X\rangle \langle X| = \int_{-\infty}^{\infty} dX |X\rangle \langle X| = 1 \quad (68)$$

and orthonormal

$$\pm\langle t|t'\rangle_\pm = \delta(t - t'), \quad \pm\langle t|t'\rangle_\mp = 0 \quad (69)$$

basis of the Hilbert space. Therefore, any quantum state can be expanded in temporal representation as

$$|\Psi\rangle = \int_{-\infty}^{\infty} dt [\Psi_+(t)|t\rangle_+ + \Psi_-(t)|t\rangle_-] = \sum_{a=\pm} \int_{-\infty}^{\infty} dt \Psi_a(t)|t\rangle_a, \quad \Psi_a(t) \equiv {}_a\langle t|\Psi\rangle. \quad (70)$$

Using their explicit expression, it is immediate to show that these eigenstates can be generated through time translations as

$$|t\rangle_{\pm} = \sqrt{\Gamma|X_R|}e^{-\frac{\Gamma t}{2}}|\pm|X_R|e^{-\Gamma t}\rangle = U(-t)\sqrt{\Gamma|X_R|}|\pm|X_R|\rangle \equiv U(-t)|0\rangle_{\pm} = e^{i\hat{K}t}|0\rangle_{\pm}. \quad (71)$$

Thus, one only needs to characterize the dynamics for the two time origins $|t=0\rangle_{\pm}$, corresponding to initial lasing amplitudes $|X = \pm X_R\rangle$, since any quantum state can be written as a superposition of time translations of those states:

$$|\Psi\rangle = \sum_{a=\pm} \int_{-\infty}^{\infty} dt \Psi_a(t)|t\rangle_a = \sum_{a=\pm} \int_{-\infty}^{\infty} dt \Psi_a(t)U(-t)|0\rangle_a = \sum_{a=\pm} \int_{-\infty}^{\infty} dt \Psi_a(t)e^{i\hat{K}t}|0\rangle_a. \quad (72)$$

As a result, the time-evolution operator simply shifts the temporal wavefunction,

$$U(t)|\Psi\rangle = \sum_{a=\pm} \int_{-\infty}^{\infty} dt' \Psi_a(t')|t'-t\rangle_a = \sum_{a=\pm} \int_{-\infty}^{\infty} dt' \Psi_a(t'+t)|t'\rangle_a. \quad (73)$$

In general, as one would expect, \hat{K} acts as $i\partial_t$ in temporal representation:

$$\hat{K}|\Psi\rangle = \sum_{a=\pm} \int_{-\infty}^{\infty} dt \Psi_a(t)\hat{K}|t\rangle_a = \sum_{a=\pm} \int_{-\infty}^{\infty} dt \Psi_a(t)(-i\partial_t)(e^{i\hat{K}t}|0\rangle_a) = \sum_{a=\pm} \int_{-\infty}^{\infty} dt i\partial_t \Psi_a(t)|t\rangle_a. \quad (74)$$

The above results apply to any density matrix $\hat{\rho}$, which can be accordingly expanded in four temporal branches as

$$\hat{\rho} = \sum_{a,b=\pm} \int_{-\infty}^{\infty} \int_{-\infty}^{\infty} dt dt' \rho_{ab}(t,t')|t\rangle_a|t'\rangle_b, \quad \rho_{ab}(t,t') \equiv {}_a\langle t|\hat{\rho}|t'\rangle_b. \quad (75)$$

The existence of such a time operator \hat{t} evades the classical no-go theorem by Pauli because the DPA Hamiltonian neither has normalizable eigenvalues nor is bounded. It can be shown that a non-degenerate parametric amplifier, which describes the dynamics of non-degenerate lasing modes, $\text{Re } \Omega \neq 0$ [45, 51], also has an associated time operator; a detailed study of the properties of the time operator emerging in parametric amplifiers is left for future work.

Late times: Phase-shift distribution

At the BdG level, any initial lasing amplitude X is exponentially amplified in time as $Xe^{\Gamma t}$, eventually dominating the dynamics. At some point, the lasing instability saturates when it becomes of the order of the condensate itself, $Xe^{\Gamma t} \sim \sqrt{n_0} \gg 1$. Once in this regime, the dynamics is described by the full GP equation. For sufficiently long times, the system approaches the CES state, where there is another time operator, \hat{t}_0 , arising from the quantum amplitude of the temporal Floquet-Nambu-Goldstone mode and describing the fluctuations of the global time origin [65]. Since the CES state is periodic, this time-shift can be expressed as an oscillation phase-shift, $\hat{\phi}_0 = -\omega\hat{t}_0$.

We now connect both time operators through the dynamics using a simple model which only involves the amplification of the lasing mode. The results of the previous subsection show that we only need to determine the evolution of the reference lasing amplitudes $\pm X_R$, since the evolution of any other initial amplitude X is obtained by adding a time-shift

$$t_0 = -\frac{1}{\Gamma} \ln \left| \frac{X}{X_R} \right|. \quad (76)$$

We assume that the reference amplitudes asymptotically yield the same CES state but with a different oscillation phase-shift that only depends on X_R , $\phi_0(X_R) = \phi_R$ and $\phi_0(-X_R) - \phi_0(X_R) = \delta$. Without loss of generality, we take

$\phi_R = 0$ as late time origin. Hence, any initial lasing amplitude X will asymptotically give rise to a CES state with a phase-shift $\phi_0(X)$ given by

$$\begin{aligned}\phi_0(X) &= -\omega t_0 = \frac{\omega}{\Gamma} \ln \left| \frac{X}{X_R} \right|, \quad X > 0, \\ \phi_0(X) &= \delta - \omega t_0 = \delta + \frac{\omega}{\Gamma} \ln \left| \frac{X}{X_R} \right|, \quad X < 0.\end{aligned}\tag{77}$$

We note that the additional phase-shift δ reflects the \mathbb{Z}_2 symmetry-breaking of a BHL at the nonlinear level [53, 54]. For computational convenience, we are not yet restricting ϕ_0 to its first Brillouin zone, $\phi_0 \in [-\pi, \pi)$, since the time-shifts arising from the initial DPA time operator \hat{t} are not bounded.

We check the above relation by simulating classical GP trajectories where the initial noise φ_W is removed from Eq. (36). This imprints a lasing amplitude $X \propto A$, which is translated into a late phase-shift ϕ_0 , from where the relation $\phi_0(X)$ can be extracted. The results are shown in Fig. 6b, in good agreement with Eq. (77). The deviations for the largest values of X can be attributed to the onset of nonlinear corrections.

In the main text, within each TW ensemble we take as reference the initial classical amplitude, $X_R = X_C > 0$, so the histograms are centered around $\phi_0 = 0$. In addition, we assume there that the fluctuations are moderate enough so that the values $X < 0$ can be neglected and $\phi_0(X)$ is an injective relation. This is for instance the case of small lasing fluctuations, $\Delta X \ll X_C$, where we find

$$\phi_0 \simeq \frac{\omega}{\Gamma} \frac{X - X_C}{X_C}.\tag{78}$$

As a result, ϕ_0 is also Gaussian, with

$$\langle \phi_0 \rangle = 0, \quad \Delta \phi_0 = \sqrt{\langle \phi_0^2 \rangle} = \frac{\omega}{\Gamma} \frac{\Delta X}{X_C} \ll 1.\tag{79}$$

We check this relation by introducing a dimensionless parameter λ that rescales the density as $n_0 \rightarrow \lambda n_0$ while leaving unchanged the rest of relevant parameters. This leads to the same mean-field evolution and same width ΔX , while the classical amplitude X_C scales as $X_C \rightarrow \lambda^{1/2} X_C$, which implies $\Delta X/X_C \rightarrow \lambda^{-1/2} \Delta X/X_C$. The corresponding TW results for the phase-shift width $\Delta \phi_0$ are shown in Fig. 6c as a function of λ for different classical amplitudes $A = 0.005, 0.01, 0.05$; the corresponding theoretical predictions (79) are depicted as solid lines. As expected, the results converge in the limit of large λ , i.e., for small $\Delta X/X_C$.

In general, the phase-shift distribution is computed from the initial lasing distribution as

$$W(\phi_0) = \int dX \delta(\phi_0 - \phi_0(X)) W_0(X),\tag{80}$$

since the relation $\phi_0(X)$ is not necessarily injective. Moreover, one also has to include the negative branch, $X < 0$.

This is the case of the strong fluctuating scenario $X_C \ll \Delta X$, which in particular includes the case of a purely quantum BHL, $X_C = 0$. In this limit, we can take $X_C \simeq 0$ and work with the normalized variable

$$z \equiv \frac{X}{\sqrt{2} \Delta X}, \quad W_0(z) = \frac{e^{-z^2}}{\sqrt{\pi}},\tag{81}$$

and choose an arbitrary reference amplitude X_R to replace the mean-field choice $X_R = X_C$. Equation (77) is then rewritten as

$$\begin{aligned}\phi_0(z) &= \phi_R + \frac{\omega}{\Gamma} \ln |z|, \quad z > 0, \\ \phi_0(z) &= \delta + \phi_R + \frac{\omega}{\Gamma} \ln |z|, \quad z < 0,\end{aligned}\tag{82}$$

with $\phi_R \equiv \frac{\omega}{\Gamma} \ln \frac{\sqrt{2} \Delta X}{|X_R|}$. The corresponding mean and variance are:

$$\langle \phi_0 \rangle = \phi_R + \frac{\delta}{2} + \frac{\omega}{\Gamma} \langle \ln |z| \rangle = \phi_R + \frac{\delta}{2} + \frac{\psi(\frac{1}{2}) \omega}{2 \Gamma} \approx \phi_R + \frac{\delta}{2} - 0.982 \frac{\omega}{\Gamma},\tag{83}$$

$$\Delta \phi_0^2 = \langle \phi_0^2 \rangle - \langle \phi_0 \rangle^2 = \left(\frac{\delta}{2} \right)^2 + \frac{\omega^2}{\Gamma^2} (\langle \ln^2 |z| \rangle - \langle \ln |z| \rangle^2) = \left(\frac{\delta}{2} \right)^2 + \frac{\psi'(\frac{1}{2}) \omega^2}{4 \Gamma^2} \approx \left(\frac{\delta}{2} \right)^2 + 1.233 \frac{\omega^2}{\Gamma^2},$$

where we have used $W_0(z) = W_0(-z)$ and

$$\langle \ln^n |z| \rangle = \int_{-\infty}^{\infty} dz W_0(z) \ln^n |z| = \frac{1}{2^n \sqrt{\pi}} \int_0^{\infty} dt \frac{\ln^n t}{\sqrt{t}} e^{-t} = \frac{\Gamma^{(n)}(\frac{1}{2})}{2^n \Gamma(\frac{1}{2})}, \quad (84)$$

$\psi(z)$ being the digamma function, i.e., the logarithmic derivative of the Euler gamma function $\Gamma(z)$,

$$\psi(z) \equiv \frac{d \ln \Gamma(z)}{dz} = \frac{\Gamma'(z)}{\Gamma(z)}. \quad (85)$$

We stress that the above distribution only depends on the \mathbb{Z}_2 -symmetry breaking phase-shift δ , and the dimensionless parameter ω/Γ , characterizing the ratio between the CES frequency and the lasing growth rate. Notice that δ only biases the distribution in such a way that, if $\omega/\Gamma = 0$, half of the events present $\phi_0 = \phi_R$ and half of the events present $\phi_0 = \delta/2 + \phi_R$. On the other hand, the reference amplitude X_R only introduces a global phase-shift ϕ_R but does not affect the width $\Delta\phi_0$. Remarkably, $\Delta\phi_0$ does not even depend on ΔX in the limit $X_C \ll \Delta X$.

Therefore, ω/Γ is the critical parameter controlling the uniformity of the late phase-shift distribution. In Figure 6d, we represent ω/Γ as a function of the initial flow velocity v in the range $v_c < v < v_{1/2}$ for fixed $c_2 = 0.4, L = 2$. It increases from the critical velocity $v_c \approx 0.82$, where $\omega = 0$, eventually diverging at $v_{1/2} \approx 0.98$, where $\Gamma = 0$.

The critical role played by ω/Γ is observed in Fig. 7, where we show the results for a purely quantum BHL with increasing $v = 0.825, 0.850, 0.900, 0.950$ (marked as red dots in Fig. 6d). Specifically, in the first row, we show the TW results for the late time ETCF. In the second row, we show the theoretical HTC prediction (89), resulting from uniformly averaging over all possible phase-shifts. As we can see, the agreement worsens close to the phase transition, where ω/Γ vanishes, indicating the absence of uniformity in the phase-shift distribution.

This conclusion is further supported by the TW histograms of ϕ_0 in third row of Fig. 7, where we observe unevenly distributed blanks in the histograms. The simple model from Eqs. (81), (82) is able to reproduce this behavior, last row of Fig. 7, where we show the histograms resulting from generating 1000 random Gaussian events for the dimensionless variable z and then evaluating $\phi_0(z)$; hereafter, we confine ϕ_0 to its first Brillouin zone $\phi_0 \in [-\pi, \pi]$ since we deal with density-based observables, which are periodic in ϕ_0 .

Hence, in order to achieve a genuine spontaneous symmetry breaking realizing all phases $\phi_0 \in [-\pi, \pi]$, it is required $\omega/\Gamma \gtrsim 1$, even in the purely quantum limit. On the other hand, ω/Γ cannot be too large since Γ close to zero implies large lasing times for the initial instability to be amplified up to the saturation regime. Thus, there is a tradeoff between lasing and spontaneous symmetry breaking. However, in practice, this tradeoff does not require a delicate fine-tuning. For instance, $v = 0.85$ (second column in Fig. 7) already displays a broad phase-shift distribution, and $v = 0.9, v = 0.95$ (third, fourth columns) are close to an ideal uniform distribution (horizontal line with error bars). In particular, the rightmost column corresponds to the simulation analyzed in the main text.

HTC correlations

At late times, expectation values can be computed using the distribution $W(\phi_0)$ from Eq. (80),

$$\langle O \rangle \simeq \int_{-\pi}^{\pi} d\phi_0 W(\phi_0) O[\phi_0], \quad (86)$$

where $O[\phi_0]$ results from evaluating the observable O by replacing $\hat{\Psi}(x, t) \simeq \Psi_0(x, \phi_0 + \omega t)$. For the density and second-order correlation function, this implies:

$$\begin{aligned} n(x, t) &= \int_{-\pi}^{\pi} d\phi_0 W(\phi_0) n_0(x, \phi_0 + \omega t), \\ g^{(2)}(x, x', t, t') &= \int_{-\pi}^{\pi} d\phi_0 W(\phi_0) n_0(x, \phi_0 + \omega t) n_0(x', \phi_0 + \omega t') - n(x, t) n(x', t'), \end{aligned} \quad (87)$$

with $n_0(x, \phi_0 + \omega t) \equiv |\Psi_0(x, \phi_0 + \omega t)|^2$. For an ideal HTC, $W(\phi_0)$ can be approximated as a uniform distribution,

$$W(\phi_0) \simeq \frac{1}{2\pi}. \quad (88)$$

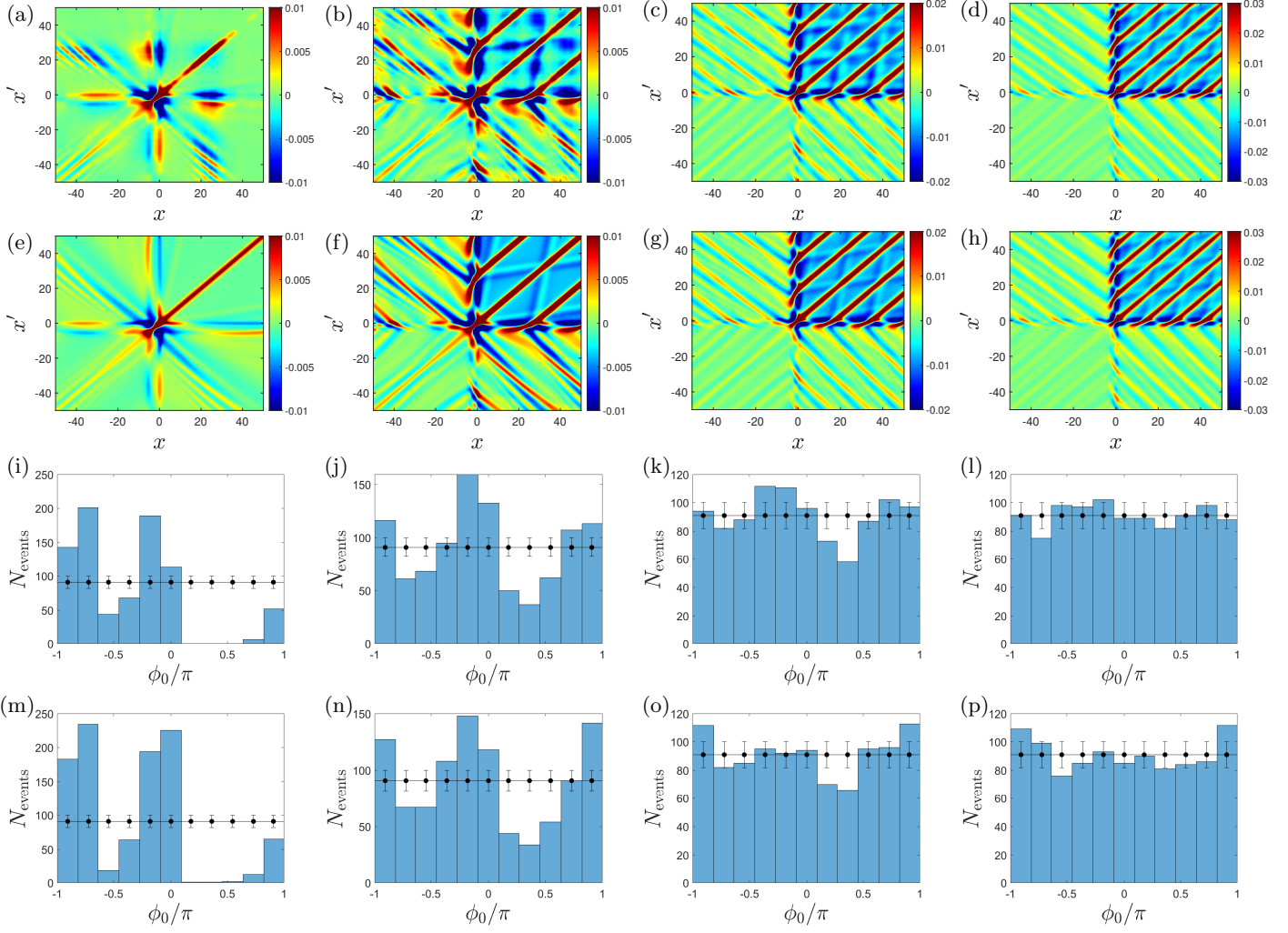


FIG. 7. (a)-(d) TW computation of the ECTF $g^{(2)}(x, x', t)$ at $t = 870$ for a purely quantum FPBHL with fixed $c_2 = 0.4$, $L = 2$ and $v = 0.825, 0.850, 0.900, 0.950$, respectively. (e)-(h) HTC prediction (89) for (a)-(d). (i)-(l) TW histogram of ϕ_0 for (a)-(d). Horizontal line with error bars: uniform distribution and its statistical uncertainty. (m)-(p) Histograms resulting from sampling 1000 random events using Eqs. (81), (82).

By combining this result with the time-periodicity of $n_0(x, t) \equiv n_0(x, \phi_0 + \omega t)$ we recover the theoretical HTC predictions of the main text:

$$\begin{aligned} n_{\text{HTC}}(x) &= \frac{1}{T} \int_0^T dt_0 n_0(x, t_0) = n_0^{(0)}(x), \\ g_{\text{HTC}}^{(2)}(x, x', \tau) &= \frac{1}{T} \int_0^T dt_0 n_0(x, t_0) n_0(x', t_0 + \tau) - n_{\text{HTC}}(x) n_{\text{HTC}}(x') = \sum_{m=-\infty}' n_0^{(-m)}(x) n_0^{(m)}(x') e^{-im\omega\tau}, \end{aligned} \quad (89)$$

where we have used the Fourier expansion of the CES density,

$$n_0(x, t) = \sum_{m=-\infty}^{\infty} n_0^{(m)}(x) e^{-im\omega t}, \quad (90)$$

and the ' denotes that the sum excludes the term $m = 0$. Hence, remarkably, the OTCF of an ideal HTC is purely oscillatory as it does not have zero Fourier component.

The spatial correlation patterns predicted in the main text are obtained by assuming that the CES density $n_0(x, t)$ is composed of traveling features in the upstream ($x < 0$) and downstream ($x > 0$) regions, $x_i(t) = x_i^{(0)} + v_i t$, where

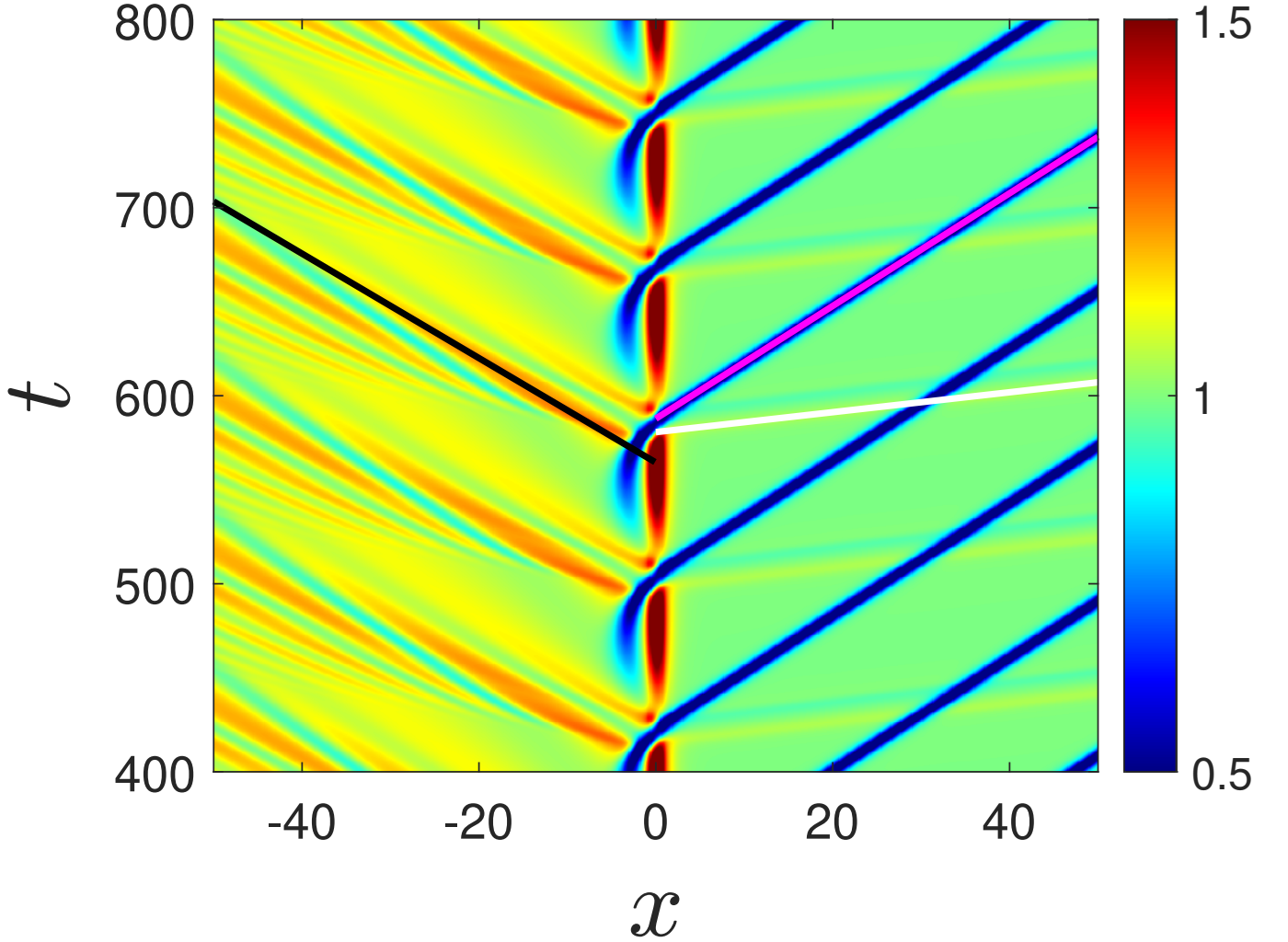


FIG. 8. CES density $n_0(x, t)$ for a mean-field simulation with $v = 0.85, c_2 = 0.4, L = 2$. Solid lines are ballistic fits of the trajectory of the upstream traveling wave (black), soliton (magenta) and downstream traveling wave (white).

$i = u, w, d$ label the upstream wave, the downstream wave and the downstream soliton, respectively. Specifically, $v_u < 0$ and $v_w > v_d > 0$, whose values are fitted from the mean-field CES wavefunction. Figure 8 shows a detailed fit of each traveling feature, where we also see that the traveling waves have a positive amplitude over the background, while the solitons carry a strong density depletion.

Consequently, we can approximate the density in the upstream/downstream region as

$$\begin{aligned} n_0(x, t) &\simeq n_u \left(t - \frac{x}{v_u} \right), \quad x < 0, \\ n_0(x, t) &\simeq n_d \left(t - \frac{x}{v_d} \right) + n_w \left(t - \frac{x}{v_w} \right), \quad x > 0, \end{aligned} \quad (91)$$

where $n_i(t + T) = n_i(t)$ are periodic functions localized around $t = -x_i^{(0)}/v_i + nT$, $n \in \mathbb{Z}$, and $n_w(t) \ll n_d(t)$ as the downstream region is dominated by the soliton emission. Their Fourier expansion reads

$$n_i(t) = \sum_{m=-\infty}^{\infty} n_i^{(m)} e^{-im\omega t}. \quad (92)$$

Therefore, we expect homogeneous and time-independent values for the average density in the asymptotic regions:

$$\begin{aligned} n_{\text{HTC}}(x, t) &\simeq \frac{1}{T} \int_0^T dt_0 n_u(t_0) = n_u^{(0)}, \quad x < 0, \\ n_{\text{HTC}}(x, t) &\simeq \frac{1}{T} \int_0^T dt_0 [n_d(t_0) + n_w(t_0)] = n_d^{(0)} + n_w^{(0)}, \quad x > 0. \end{aligned} \quad (93)$$

Regarding the second-order correlation function, we define

$$\begin{aligned} g_{ij}(x, x', \tau) &\equiv g_{ij}(\tau_{ij}) \equiv \frac{1}{T} \int_0^T dt_0 n_i(t_0) n_j(t_0 + \tau_{ij}) - n_i^{(0)} n_j^{(0)} = \sum_{m=-\infty}^{\infty} n_i^{(-m)} n_j^{(m)} e^{-im\omega\tau_{ij}}, \\ \tau_{ij} &\equiv \tau + \frac{x}{v_i} - \frac{x'}{v_j}. \end{aligned} \quad (94)$$

It is immediate to see that $g_{ij}(\tau_{ij})$ is localized around $\tau_{ij} = \frac{x_i^{(0)}}{v_i} - \frac{x_j^{(0)}}{v_j} + nT$, $n \in \mathbb{Z}$, which implies that $g_{ij}(x, x', \tau)$ is localized in the (x, x') plane around the equispaced, parallel bands

$$\frac{x'}{v_j} - \frac{x}{v_i} = \frac{x_j^{(0)}}{v_j} - \frac{x_i^{(0)}}{v_i} + \tau + nT. \quad (95)$$

This yields Eqs. (6), (7) in the main text. Specifically,

$$\begin{aligned} g_{\text{HTC}}^{(2)}(x, x', \tau) &\simeq g_{uu}(x, x', \tau), \quad x, x' < 0, \\ g_{\text{HTC}}^{(2)}(x, x', \tau) &\simeq g_{ud}(x, x', \tau), \quad x < 0, \quad x' > 0, \\ g_{\text{HTC}}^{(2)}(x, x', \tau) &\simeq g_{du}(x, x', \tau), \quad x > 0, \quad x' < 0, \\ g_{\text{HTC}}^{(2)}(x, x', \tau) &\simeq g_{dd}(x, x', \tau) + g_{dw}(x, x', \tau) + g_{wd}(x, x', \tau), \quad x, x' > 0. \end{aligned} \quad (96)$$

The self-correlations of the upstream waves and the downstream solitons are described by the g_{uu} and g_{dd} functions, while the analogue of the Hawking and Andreev correlations are encapsulated in the g_{ud} , g_{du} and g_{wd} , g_{dw} functions, respectively. The correlations g_{uw} , g_{wu} , g_{ww} are neglected as they are too weak to be observed, in analogy to the subdominant character of the normal-normal $u - d1$ correlations from the Hawking effect [27].

We also evaluate the spatial Fourier transform of the OTCF within a certain region $\mathcal{R} \in \mathbb{R}^2$,

$$g^{(2)}(k, k', t, t') = \int_{\mathcal{R}} dx dx' g^{(2)}(x, x', t, t') e^{-ikx} e^{-ik'x'}. \quad (97)$$

In practice, we take the region \mathcal{R} as one of the four quadrants of the Cartesian plane. Consequently, from Eq. (96), we only need to compute the Fourier transform of $g_{ij}(x, x', \tau)$, which is expected to exhibit a discrete peak structure from Eq. (94),

$$g_{ij}(x, x', \tau) = \sum_{m=-\infty}^{\infty} g_{ij}^{(m)}(\tau) e^{-im\frac{\omega}{v_i}x} e^{im\frac{\omega}{v_j}x'}, \quad g_{ij}^{(m)}(\tau) = n_i^{(-m)} n_j^{(m)} e^{-im\omega\tau}. \quad (98)$$

In the main text, we focus on the downstream-upstream region $\mathcal{R} = (0, \infty) \times (-\infty, 0)$, where the analogue of the Hawking correlations are exhibited between the upstream waves and the downstream solitons. In particular, we evaluate $g^{(2)}(x, x', t, t')$ at the peak of the upstream/downstream spectrum, $k_{u,d} = \frac{\omega}{|v_{u,d}|}$. For an HTC, we obtain

$$g_{\text{HTC}}^{(2)}(k_d, k_u, \tau) \simeq g_{du}^{(-1)}(\tau) = n_d^{(1)} n_u^{(-1)} e^{i\omega\tau}. \quad (99)$$

Thus, the HTC prediction for the figure of merit in the main text is just

$$\mathcal{G}_{\text{HTC}}(\tau) = \frac{g_{\text{HTC}}^{(2)}(k_d, k_u, \tau)}{g_{\text{HTC}}^{(2)}(k_d, k_u, \tau = 0)} = e^{i\omega\tau}. \quad (100)$$

In Fig. 9, we compare this prediction with the TW simulation in Fig. 2k of the main text in more detail, finding an excellent agreement.

We remark that the approximate nature of these expressions, which can be traced back to Eq. (91), stems solely from the dispersion of the upstream and downstream waves (especially in the upstream case), while the traveling character of a soliton train is instead *exact*.

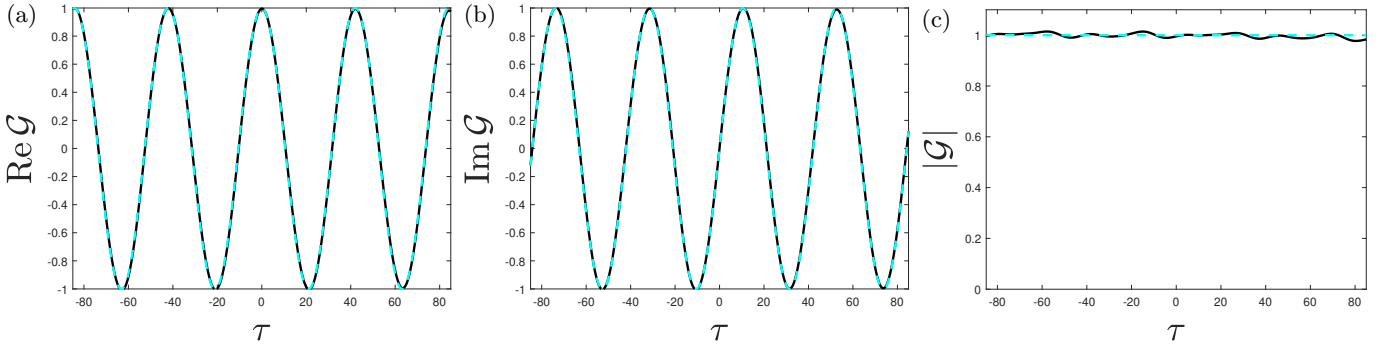


FIG. 9. Figure of merit $\mathcal{G}(\tau)$ for a purely quantum FPBHL with $v = 0.95$, $c_2 = 0.4$, $L = 2$ (see Fig. 2k of main text), computed via TW method (solid black) versus theoretical prediction $\mathcal{G}_{\text{HTC}}(\tau) = e^{i\omega\tau}$ (dashed cyan). (a) Real part $\text{Re } \mathcal{G}(\tau)$. (b) Imaginary part $\text{Im } \mathcal{G}(\tau)$. (c) Absolute value $|\mathcal{G}(\tau)|$.

Experimental effects

We now discuss explicitly the inclusion of realistic experimental effects, such as finite temperature and experimental noise. In actual experiments, the main source of noise are run-to-run fluctuations in background parameters such as particle number or the confining potential, whose main effect is to add a stochastic component to the amplitude of the deterministic background Bogoliubov-Cherenkov-Landau (BCL) radiation [41, 62, 100, 101].

We can model the effect of BCL fluctuations by adding a stochastic component to the classical amplitude A in the initial TW condition (36), $A \rightarrow A + \delta A$, with δA a random variable with zero mean, $\langle \delta A \rangle = 0$, and statistical deviation $\sqrt{\langle \delta A^2 \rangle} = \Delta A$. The BCL fluctuations increase the width ΔX of the lasing amplitude. Specifically, from Eq. (51), we now have that

$$\hat{X} = X_C + \delta X_C + \frac{1}{\sqrt{L}} \sum_k \beta_k \hat{\alpha}_k + \beta_k^* \hat{\alpha}_k^\dagger, \quad \delta X_C \equiv i(z_S|\Phi_C)\sqrt{n_0} \delta A. \quad (101)$$

As a result, we still have $\langle X \rangle = X_C$ but now [see Eq. (57)]

$$\Delta X^2 = \Delta X_C^2 + \Delta X_T^2 + \Delta X_Q^2, \quad \Delta X_C^2 = |(z_S|\Phi_C)|^2 n_0 \Delta A^2. \quad (102)$$

Hence, the main effect of including finite temperature and experimental noise is to enhance the fluctuations of the lasing mode, which further randomizes the asymptotic phase-shift ϕ_0 . Moreover, if we assume that the BCL noise is Gaussian, the Wigner distribution for X will be still a Gaussian of the form (56), with ΔX given by the equation above. Therefore, all our previous results still apply even when including experimental effects.

Figure 10 shows the results of including finite temperature and experimental fluctuations in the TW method. In the first two columns, we show the effect of a finite temperature $T = 0.5$ combined with some BCL noise $\Delta A = 0.005, 0.002$ around a finite classical amplitude $A = 0.01, 0.005$, respectively. We observe that the ETCF in the first row are quite close to the ideal case, as can be also inferred from the broad histograms in the second row. These can be compared with the results of including only quantum fluctuations shown in the main text, presenting much narrower distributions.

The third column represents the more realistic simulation, where $T = 0$ and only pure BCL noise is added to the initial quantum fluctuations, $A = 0$ and $\Delta A = 0.01$. This is the type of model that successfully reproduced the experimental results in Ref. [41], in which the effect of temperature was found to be negligible and BCL fluctuations were sufficiently strong to stochastically stimulate Hawking radiation. We observe that the agreement with an ideal HTC is quite good.

Indeed, the main impediment to observe the BHL effect in current experiments is the strong background of fluctuating BCL radiation, which overshadows the lasing amplification in its early stages. This would correspond to set $\Delta A \sim 1$ in the above mentioned simulation, so the initial state is no longer close to a BHL configuration. Nevertheless, a detailed analysis of experimental effects is beyond the scope of the present work since that will depend on the specific setup proposed for the achievement of the BHL, which remains as one of the biggest present challenges in the field of analogue gravity.

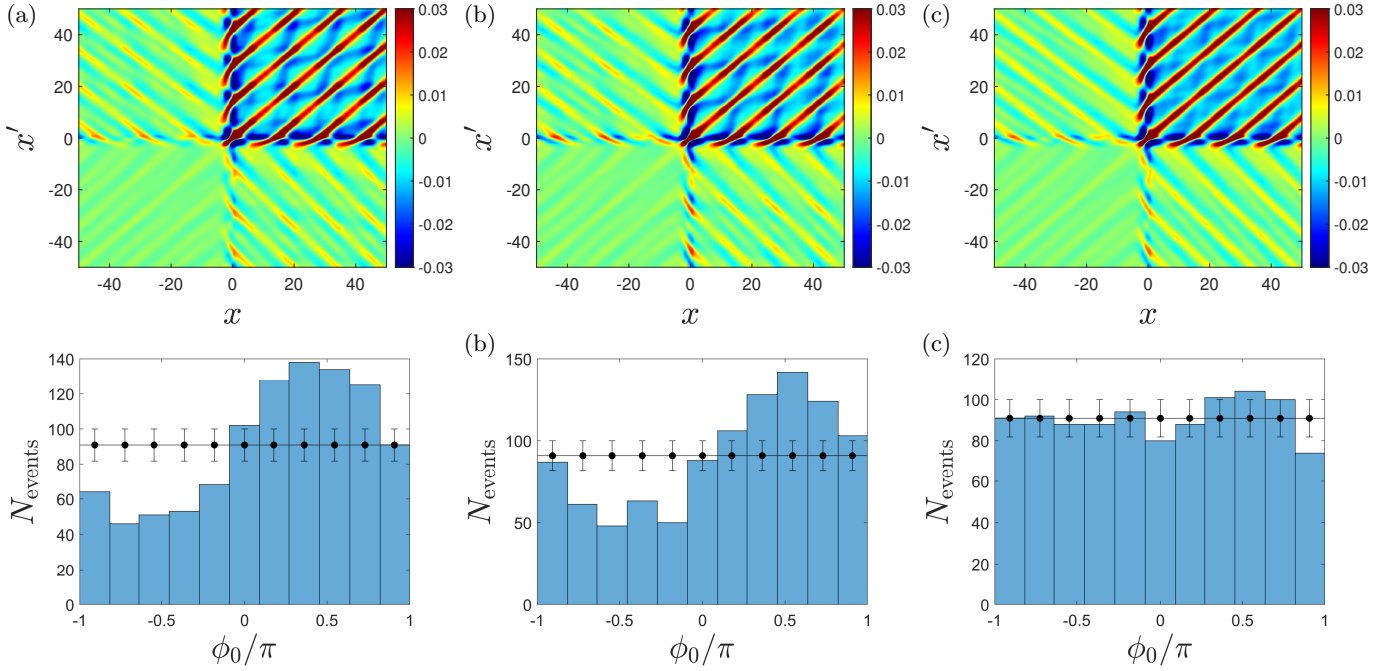


FIG. 10. (a)-(c) Realistic TW computation of the ECTF $g^{(2)}(x, x', t)$ at $t = 870$ for a FPBHL with $v = 0.95$, $c_2 = 0.4$, $L = 2$, including finite temperature T and experimental noise in the classical amplitude. The corresponding values are $T = 0.5, 0.5, 0$, $A = 0.01, 0.005, 0$, and $\Delta A = 0.005, 0.002, 0.01$. (d)-(f) TW histogram of ϕ_0 for (a)-(c). For the simulation in (c), where $A = 0$, the time reference is chosen from a mean-field simulation with $A = 0.003$.